

**BUILDING THE THIRD-GENERATION CORNELL MAGNETIC
RESONANCE FORCE MICROSCOPE****6.1 Introduction**

At the time of writing this thesis, a third-generation magnetic resonance force microscope (Figure 6.1) is in the final stages of construction and testing at Cornell University. The previous-generation microscope [79] enabled a number of exciting advances in spin detection protocols [30, 61, 88] and cantilever fabrication [81, 82]. However, multiple serious limitations prevent its continued use as we pursue three-dimensional imaging experiments and study sensitivity-enhancement techniques, such as dynamic nuclear polarization (DNP) [152] and Fourier-transform MRFM (FT-MRFM) imaging [76].

The largest motivating factor for building the new microscope was to change from only being able to scan the cantilever in one (vertical) dimension to instead having full three-dimensional scanning capabilities. In addition to needing three dimensions of motion to obtain three-dimensional images [12], lateral stage motion also is required to position magnet-tipped cantilevers over low-power, 1-10 μm wide radiofrequency (rf) field sources [60]; micrometer-wide transmission lines generate large transverse fields, which are essential to generate sufficiently large transverse magnetic fields for high-sensitivity MRFM experiments. A second goal was to increase the hold time of the liquid helium dewar from 2.5 days to at least 5 days, which would provide significantly more time for uninterrupted measurements between helium fills. Additionally, definitive studies of the transfer of polarization from electron spins to nuclear spins by DNP in an MRFM experiment will require a double-resonance apparatus that can simultaneously apply microwaves (to polarize electron spins) and radiowaves (to read out the transfer to nuclear spins). The previous-generation micro-

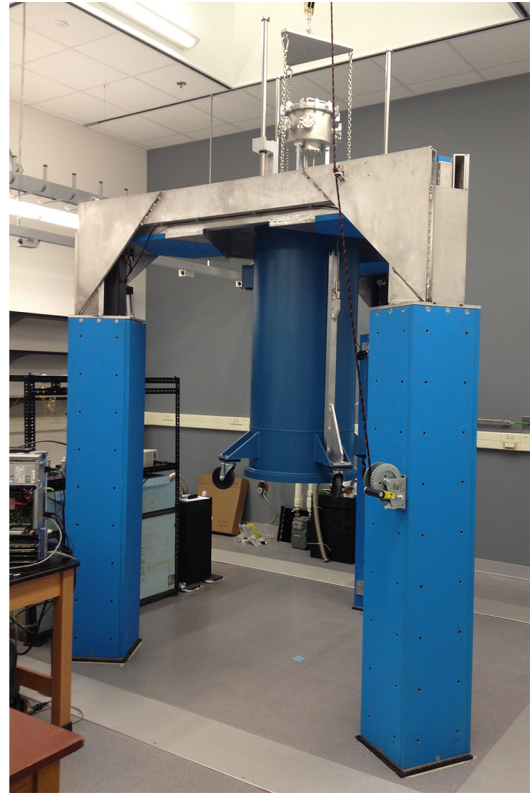
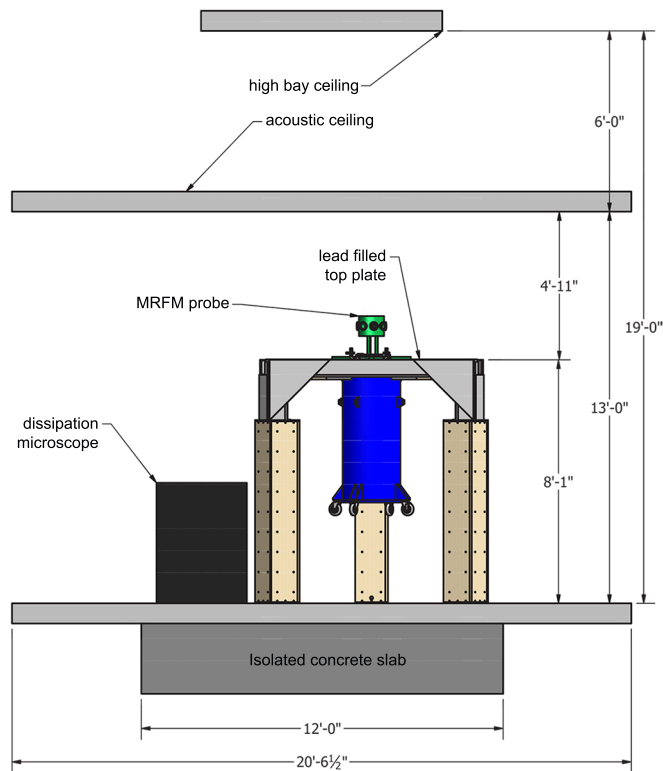


Figure 6.1: Third-generation MRFM microscope superstructure. The microscope is designed to operate in a vacuum of 10^{-6} mbar, at a temperature of 4.2 K, and in magnetic fields up to 9 T. Left: Schematic of the microscope inside the PSB B19 laboratory at Cornell University. The MRFM microscope was positioned over a concrete slab that is isolated from the building foundation. The room's ceiling is 19 ft tall, and the false ceiling surrounding the perimeter of the room is 13 ft. The superstructure consists of a lead-filled top plate that is suspended by air springs attached to three wooden legs filled with sand. The MRFM probe bolts to the top side of the top plate and inserts into a 9 T cold-bore magnet housed inside of a liquid helium dewar (blue). The dewar is bolted to the underside of the top plate. The probe is connected to a high-vacuum chamber (green), and pump lines run from this chamber to a turbomolecular pump located in an adjacent service chase. Right: Image of the probe superstructure with the dewar and microscope bolted to the top plate.

scope had room for only one coaxial cable to be fed through to the probe head, which did not allow for the simultaneous irradiation of electrons and nuclei through separate lines, and the use of a power splitter to feed radiowaves and microwaves through the same line caused significant electrical cross-talk. Improvements to heat-sinking were also desired; the previous microscope required a $50\ \Omega$ termination within the probe head and had no heat sinking to the center line of the coaxial cable, both of which caused significant heating. Furthermore, we hoped to improve the vibrational isolation of the microscope by building the new microscope in a new, ground-floor laboratory. The second-generation microscope rested on a light aluminum plate supported by three air-hydraulic legs and was in a room with significant acoustic noise that was located two levels above the building foundation. This configuration did not provide sufficient vibrational isolation to prevent environmental vibrations from exciting the commercial Attocube nanopositioner used for vertical cantilever motion (Attocube Systems AG, ANPx51/HV/LT). The third-generation microscope has been constructed in an rf-shielded laboratory on an isolated concrete slab on the ground floor of the newly-constructed Cornell Physical Sciences Building (PSB), which has been shown to provide far superior vibrational isolation (see Section 6.2.1).

The third-generation microscope is designed to operate at a temperature of 4.2 K, in a vacuum of 10^{-6} mbar, and in magnetic fields up to 9 T. These specifications have placed stringent constraints on the microscope design. The subsequent sections of this chapter include a discussion of the key features of the microscope superstructure, MRFM probe body, and the probe head. Note that the “probe head” refers to the portion of the microscope contained within the vacuum can, and primarily includes the sample platform, cantilever mount, and 3D scanning stage; the MRFM “probe body” refers to the vacuum-compatible support system for the probe head; and the “microscope superstructure” refers to all of the large-scale features of the microscope that are not under vacuum, such as the vibrational isolation platform, the liquid helium dewar, and the hoist system. Note also that throughout

this chapter, the unit of inches is denoted with a double prime; for example, 3 inches = 3”.

6.2 MRFM Microscope Superstructure

The superstructure of the third-generation MRFM microscope can be seen in Figure 6.1. The microscope frame consists of a lead-filled top plate that is suspended by air springs on sand-filled legs. 1,000 lb of sand was divided evenly between the three legs. Very similar designs have been successfully used to decouple the microscope from environmental vibrations in scanning tunneling microscopes (STMs) [153, 154]. A liquid helium dewar containing a 9 T superconducting magnet, which supplies the external field in our MRFM experiments, is bolted to the underside of this floating, lead-filled top plate. The MRFM probe bolts to the top of the floating plate and inserts into the dewar so that the probe head, and specifically the cantilever and sample, are centered in the bore of the 9 T magnet. This section details the vibrational isolation of the MRFM microscope, the design specifications of the low-loss dewar, and a dual hoist system for the MRFM probe and the dewar.

6.2.1 Vibrational Isolation of the MRFM Microscope

Vibrational isolation of the sample and cantilever from the surrounding environment is essential to achieve a reasonable signal-to-noise ratio (SNR) in an MRFM experiment. Multiple levels of vibrational isolation were used in this third-generation microscope. The microscope was built in a room in the newly-completed Physical Sciences Building at Cornell University. Unlike our previous laboratory, which was located two floors above ground level, the new room is on the ground floor of PSB. The microscope is located on a concrete slab that is separate from the foundation of the building. The room is also rf-shielded, and acoustic

noise is minimized by having the vacuum pump located in an adjacent service chase.

To assess the improvement in vibrational isolation in the new laboratory, a geophone (Geospace Technologies) was used to compile vibrational data both for the second-generation microscope (in Baker 146) and for the new microscope (in PSB B19). Details on the calibration and use of a geophone are detailed in Appendix B of Ref. 155. In Baker 146, data were recorded on the floor of the room and on the floating aluminum plate that was used for vibrational isolation of the magnetic resonance force microscope. In PSB B19, data were recorded on the floor of the main portion of the room that is connected to the building foundation and on the isolated concrete slab. The collected data, shown in Figure 6.2, indicate that even just the building foundation in PSB B19 experienced significantly fewer vibrations compared to the floating aluminum plate in the previous laboratory. Vibrations were further reduced on the isolated concrete slab in PSB B19. These measurements can be compared to the vibrational profiles observed in six STM laboratories around the United States in Figure B.9 of Ref. 155; our laboratory's ambient vibration noise is observed to be comparable to, or slightly better than, the vibrations seen in many of these state-of-the-art STM laboratories.

The microscope frame consists of three 6 ft tall wooden legs that were braced with aluminum angle and each filled with sand. Hydraulic air springs were bolted to the tops of the legs, and the air springs support a top plate consisting of an aluminum frame with three triangular-shaped wells that each contain ten 25 lb bags of lead shot (totaling 750 lb of lead in the top plate). During MRFM measurements, the MRFM probe and liquid helium dewar are bolted to the top side and underside of the suspended top plate, respectively.

Decoupling vibrations that could pass through tubing and wires was also essential. All fiber optic cables and electrical wires were damped with weighted-down foam on the top plate before they were connected to the MRFM probe. Vibrations through the pumping

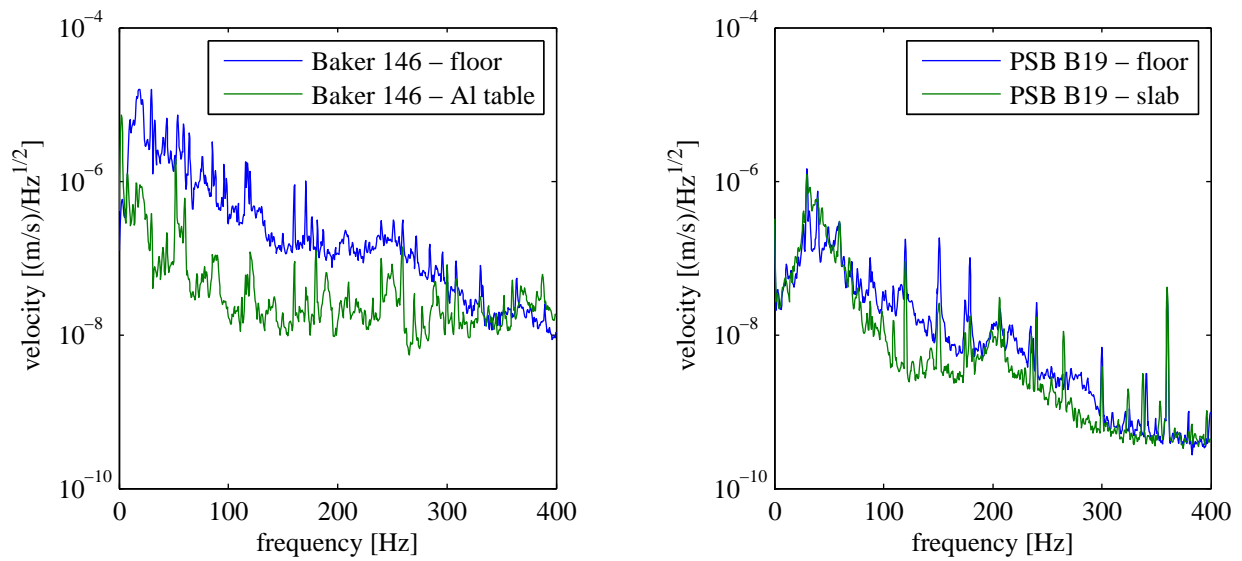


Figure 6.2: Vibrational measurements from the room that housed the second-generation MRFM microscope (Baker 146) and the room that now houses the third-generation microscope (PSB B19); both laboratories are at Cornell University. Left: Vibrational data on the floor (blue) and on the floating aluminum vibrational-isolation plate (green) in Baker 146. Baker 146 was two stories above the ground level of the building. Right: Vibrational data on the floor connected to the building foundation (blue) and on the floor of the isolated concrete slab (green) in PSB B19. The data indicate that the new laboratory in PSB has superior vibrational isolation from the environment.

line connected to the turbomolecular pump, which could induce significant vibrations, were decoupled using a multi-step approach. To mitigate acoustic vibrations the vacuum line was passed from the pump, which was stored in an adjacent service chase, into the laboratory by running 1.5" outer diameter (OD) stainless steel tubing through a 1 ft thick concrete wall. The vibrations were further damped by passing the line through additional solid stainless steel tubing in a concrete box and by bolting tubing to the side of the sand-filled wooden leg and the top plate using vibration-damping clamps. Between each bolted portion of solid tubing, flexible bellows of various lengths with NW-40 connectors on either side were used (Kurt J. Lesker Company; example part that was 36" long is MH-QF-C36). All pieces of solid tubing (1.5" outer diameter) were made of stainless steel and had stainless-steel-bored NW-40 flanges (Kurt J. Lesker Company, part QF40-150-SBB) welded to either end.

6.2.2 Narrow-Neck Liquid Helium Dewar

A new liquid helium dewar was purchased for this microscope to house the cold-bore 9 T superconducting magnet that supplies the external magnetic field in the MRFM experiments. The magnet has a 4" wide bore. For the new system the helium loss rate, with the MRFM probe inserted, was sought to be decreased from 20 L/day (the rate for the previous dewar) to less than 10 L/day. Since the new dewar has a liquid helium reservoir of 50 L, a loss rate of 10 L/day would correspond to a 5 day hold time. Five days between helium fills would provide sufficient uninterrupted measurement time to enable data collection for three-dimensional MRFM image reconstruction.

The high helium boil-off rate in the previous dewar was attributed primarily to the top loading design of the dewar, which required a 10" wide neck so that the superconducting magnet could be lowered to the base of the dewar from the top. Although the magnet insert included baffles to minimize blackbody radiation, it was expected that narrowing the width

of the neck would significantly improve the hold time.

The new dewar, which was purchased from American Magnetics Inc. (AMI) and manufactured by Kadel Engineering Corp, has a narrow 4" diameter neck that matches the 4" diameter bore of the superconducting magnet. The neck diameter could not be further reduced since the vacuum can at the base of the MRFM probe, which inserts into the dewar, has a 3.5" outer diameter. Schematics of the narrow-neck dewar are shown in Figure 6.3. The dewar is vapor shielded with multilayer superinsulation. A vapor-shielded dewar was chosen instead of a nitrogen jacket to prevent vibrations induced by boiling nitrogen; however, other MRFM labs have used dewars with nitrogen jackets without noticeably increased vibrational noise [156]. The neck of the dewar, which is the region between the top flange and the liquid helium reservoir, is made of low thermal conductivity fiberglass G-10 to promote thermal isolation. High temperature superconductor (HTS) current leads were installed to minimize the thermal loads of the leads; since the magnetic field is often swept in the MRFM experiments, HTS fixed leads were preferred over break-away leads. A custom centering puck with a 45° taper was fabricated at the base of the dewar. During measurements the base of the can, which has a matching 45° taper, is set down into the centering puck to prevent pendulum motion of the probe head. Casters and lifting lugs were required for movement of the dewar into position under the superstructure top plate. Note that since the lifting lugs were fabricated out of specification (at the wrong vertical position), custom stainless steel bars with lifting lugs lowered to the correct vertical position were retrofitted on the dewar. A helium level monitor was built into the dewar. The dewar has a 0.5" diameter helium fill port, which also is used to pre-cool with liquid nitrogen. The dewar has two NW-25 ports; one port is connected to a 5 psi relief valve, and the second is connected to Cornell University's helium recovery system.

The helium loss rate without the MRFM probe insert was quoted by AMI to be 0.187 L/hr,

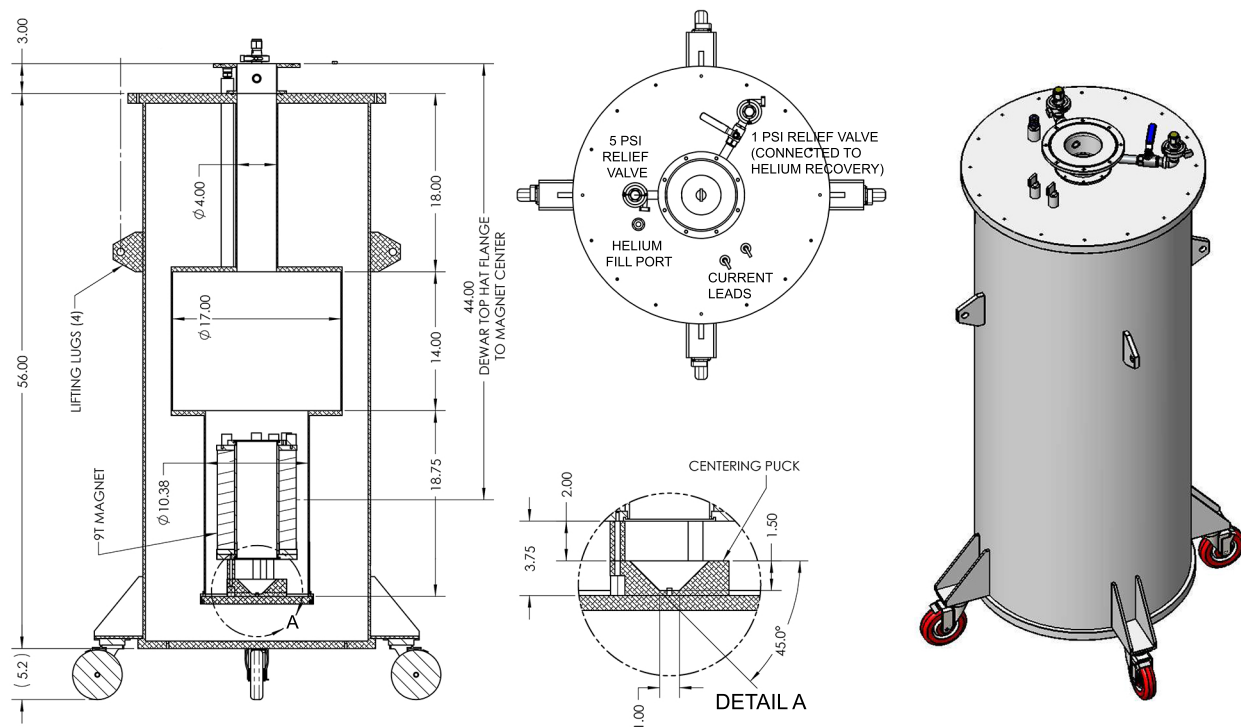


Figure 6.3: Schematics of the bottom-loading liquid helium dewar that contains a 9 T superconducting magnet. Left: Cross-section of the dewar detailing the relevant dimensions for the neck of the dewar, 50 L liquid helium reservoir, and cold-bore magnet. Top center: Top-down view of the dewar, which shows the top hat that mates to the MRFM probe (center), relief valves, liquid helium fill port, and current leads. Bottom center (Detail A): Details for the centering puck at the base of the dewar, which was designed to mate to the base of the MRFM probe vacuum can to mitigate pendulum motion of the probe head. Right: Three-dimensional schematic of the dewar.

which corresponds to 4.5 L/day. After inserting the MRFM probe, the loss rate immediately after the first helium fill was measured to be approximately 20 L/day. However, after the system had reached the base temperature of 4.2 K and after the second fill, the loss rate was measured to be approximately 7 L/day (without running the superconducting magnet). Once the MRFM probe is operational, additional data will need to be collected to approximate the losses while running the magnet. However, these initial results, which indicate a hold time of 7 days, are very encouraging.

6.2.3 Dual Hoist System

A hybrid movable/fixed probe setup was designed to provide the best combination of system performance and ease of access to the probe head between thermal cycles, given the constraint that a pit could not be installed in the laboratory. When the probe is bolted to the top plate, the dewar is too tall to be moved underneath the probe. Since the construction of a taller frame could introduce low-frequency vibrational modes into the microscope superstructure, the probe was designed to be lifted, but only to a controlled height and while always remaining rigidly supported. Prior to positioning the dewar, the probe is controllably hoisted 2.5 ft, which provides 6" of clearance between the dewar and the base of the vacuum can on the probe. The probe, which is bolted to a three-armed plate, is raised and lowered by gliding linear bearings in C-shaped clamps attached to the ends of the arms along stainless steel shafts. The shafts are rigidly fixed, so the probe can be smoothly hoisted vertically without any lateral displacement. Electrical and vacuum connections remain attached to the probe when it is being raised and lowered. Details of this guide system are shown in Figure 6.4.

To assemble and bolt the dewar and the MRFM probe to the top plate prior to filling with liquid helium, two hoists are used. The probe (with the vacuum can in place) is first

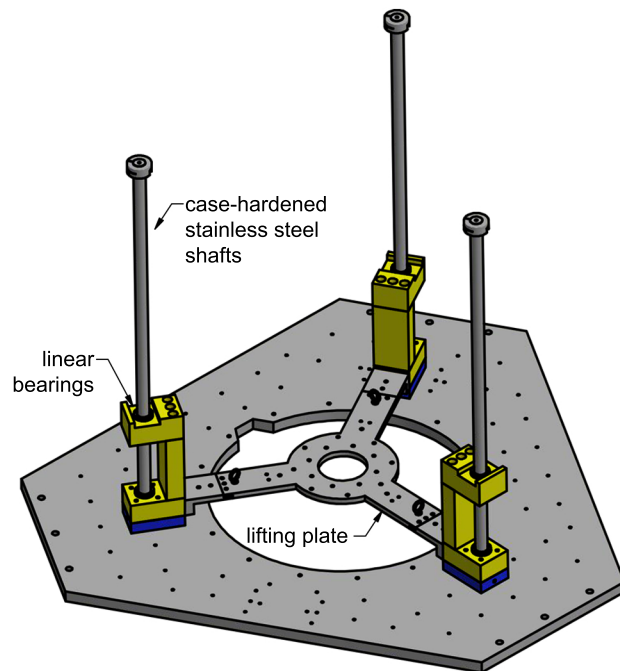


Figure 6.4: Hoist system for the MRFM probe. A hybrid movable/fixed probe hoist design was achieved by gliding the probe along case-hardened stainless steel shafts. A three-armed lifting plate was designed with C-shaped clamps at the end of each arm; the MRFM probe is bolted to this lifting plate. Two sets of linear bearings were placed in each C-shaped clamp, which are used to rigidly fix the lateral position of the MRFM probe. A single hoist point was affixed to the top of the MRFM probe vacuum chamber to lift the probe. When the hoist point is pulled, the linear bearings glide along the shafts and the probe is smoothly raised 2.5 ft, which provides sufficient clearance between the dewar and the bottom of the probe. Left: Image of the hoist plates that shows the hoist point connected to the center of the vacuum chamber lid. Right: Schematic of the lifting components, including the lifting plate, C-shaped clamps (yellow), linear bearings, and stainless steel shafts.

raised by a hoist point centered on the lid of the vacuum chamber at the top of the MRFM probe. A nylon rope connected to the hoist point goes through a block-and-tackle pulley system with a mechanical advantage of 4:1 in the ceiling of the room and then is routed to a winch located on one of the legs of the superstructure frame. Once the probe is raised, the dewar is brought into position under the probe. The dewar is raised by two lift points (lifting lugs) on the sides of the dewar. One stainless steel rope connects to both lifting lugs, and the center of this rope is hauled by a pulley that is connected to a second, larger winch with a mechanical advantage of 10 \times . After the dewar is raised and bolted to the underside of the top plate, the probe is lowered until the base of the vacuum can is centered in the centering puck at the base of the dewar. The probe is then also bolted into place.

The nylon rope connected to the MRFM probe vacuum chamber is removed during experiments; however, the wire rope is expected to remain connected to the dewar during measurements, with slack in the line to minimize the transmission of vibrations from the probe superstructure to the dewar. The wire rope and connectors to the lifting lugs therefore must be non-magnetic. Type 305 stainless steel wire rope with a 0.25" diameter (breaking strength of 4,900 lb) was purchased from McMaster Carr for this purpose. The wire rope fittings are Electroline Machined Series Clevis Socket Fittings (part IS-125; breaking strength 6,800 lb) purchased from Metro Industrial Supply, LLC.

6.3 Third-Generation MRFM Probe Body

The primary purpose of the long, thin MRFM probe body is to position the sample and cantilever for the MRFM experiment in the center of the bore of the 9 T superconducting magnet. The probe must be compatible with the constraints of the experiment, including working in high magnetic fields, at cryogenic temperatures down to 4.2 K, and in high

vacuum between the temperature range of 293 K and 4.2 K. High magnetic fields require the use of non-magnetic components. Choosing appropriate materials to account for thermal contraction and to mitigate thermal losses was essential. Maintaining high vacuum required the prevention of outgassing or virtual leaks, as well as the use of cryo-compatible welds and solder joints. A second function of the MRFM probe body is to transition all wires, fiber optic cables, and coaxial cables needed for the MRFM experiment into vacuum and to heat-sink them before they reach the cryogenically cooled experimental components in the probe head. In this section, details are provided for the vacuum-compatible probe body design, vacuum feedthroughs, and the use of baffles to mitigate blackbody radiation.

6.3.1 Vacuum-Compatible MRFM Probe Body Design

The MRFM probe body is shown in Figure 6.5. The “probe plate” is used to make an air-tight seal between the probe and the liquid helium dewar; everything above the probe plate is at room temperature, whereas the underside of the probe plate and everything beneath are sealed in the liquid helium dewar. Above the probe plate is a 10” OD cylindrical vacuum chamber with seven NW-40 vacuum ports (6” tall; approximate volume $V = 490 \text{ in}^3$; manufactured by Kurt J. Lesker Company). The chamber was designed to store spare fiber optic cables and electrical wires; for easy access to the inside of the chamber, an ISO-K 250 flange was installed as the lid to the chamber. Feedthroughs for the fibers and wires were attached to NW-40 blank flanges and connected to the ports on the vacuum chamber. One of the NW-40 ports is also used as the connection point for the turbomolecular vacuum pump. Three thin-walled type 304 stainless steel vacuum tubes connect this chamber to the vacuum can at the bottom of the MRFM probe. Two of the tubes have an OD of 7/16” and the third tube has an OD of 5/8”; all tubes have wall thicknesses of 0.035” and are 47.5” long. The vacuum tubes were welded to a 6” OD conflat (CF) flange at the base of the vacuum

chamber, to the probe plate (to transition to the inside of the liquid helium dewar), and to the top of the vacuum can.

Once inside the liquid helium dewar, blackbody radiation is mitigated using copper baffles [157]; further details on the baffles are provided in Section 6.3.3. At the base of the MRFM probe is the vacuum can. The vacuum can has a grease seal with a 10° taper and an overlap length of approximately 0.625" between the inner and outer halves of the seal. This angle was designed to be slightly shallower than the 14° taper for the second-generation probe to make it easier to disassemble the vacuum can; the overlap length was consistent between the two probes. The top of the can (the inside half of the grease seal) was made of stainless steel; the outer half of the grease seal was made of brass. The main body of the vacuum can was made from 3.5" diameter copper tubing (wall thickness 0.064") and the base of the vacuum can, which was made of brass, was tapered at a 45° angle to align with the centering puck at the base of the dewar. The 16.25" long vacuum can (when empty) has an approximately volume $V = 150 \text{ in}^3$. The brass and copper components of the can were soldered together with silver solder.

Extra tolerance in the length of the probe, so that the base of the vacuum can could properly align with the dewar centering puck, was achieved by positioning an edge-welded bellows between the probe plate and the dewar. Airtight seals between the probe components and the bellows were maintained using ISO-100 (4" inner diameter) vacuum flange connections. The bellows was custom manufactured by Bellows Tech, LLC.

To facilitate disassembly of the vacuum can after it has been sealed to the probe body, a removal assembly was designed, as shown in Figure 6.6. Three rods bolt to the stainless steel top of the can and approach a ring that is attached to the base of the vacuum can. Set screws in the top rods are slowly pushed against the ring to release the vacuum can. Note that it is essential to hold the base of the vacuum can when releasing it, since it releases

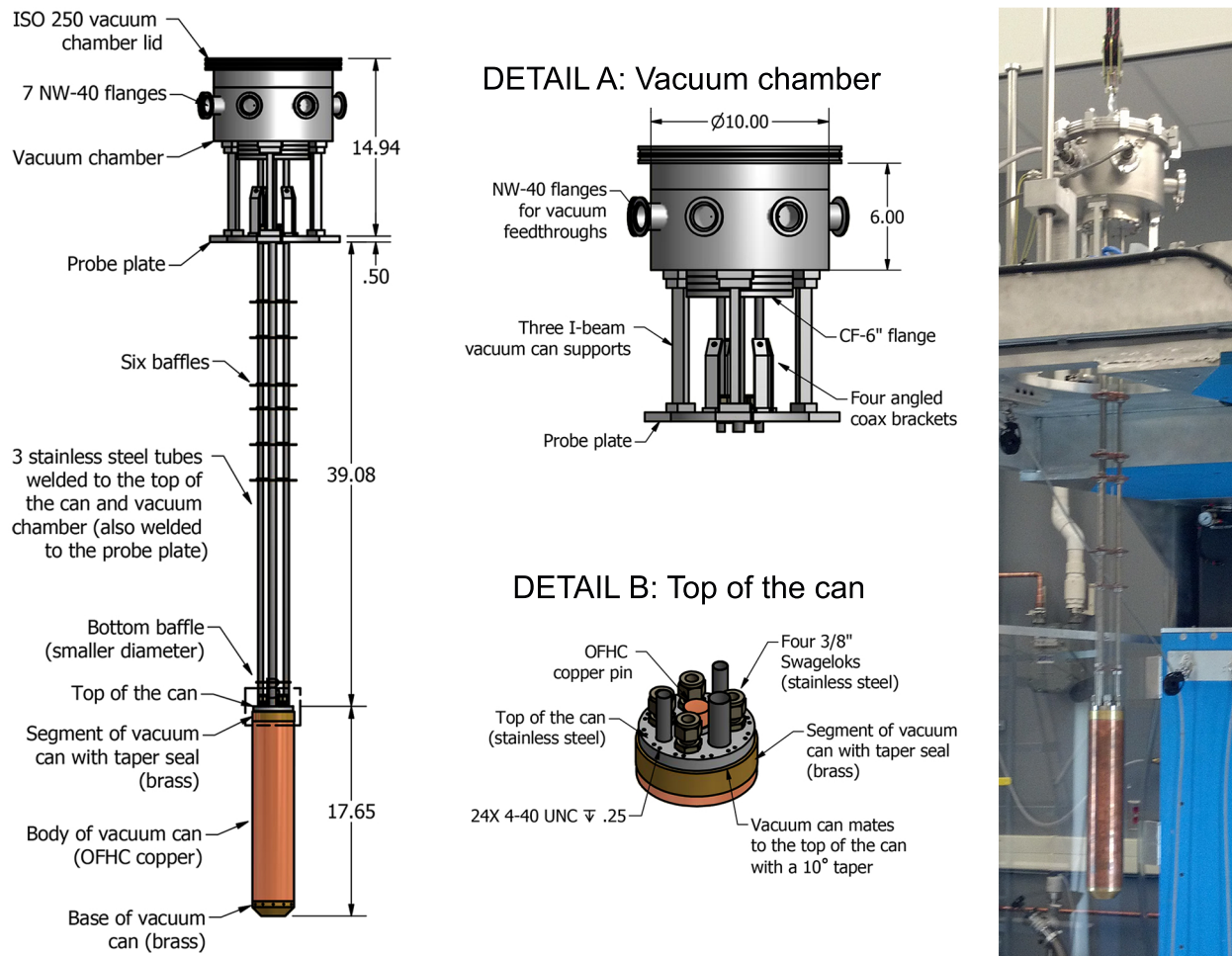


Figure 6.5: Third-generation MRFM probe body. Left: Schematic of the probe body, detailing critical dimensions and describing the key components. Note that three thin-walled stainless steel tubes were welded to the CF-6" flange at the base of the vacuum chamber, to the probe plate, and to the top of the can. Six copper baffles were installed between the probe plate and the top of the can, with an additional bottom baffle located near the vacuum can to guide the coaxial cables into the Swagelok feedthroughs. Detail A: Detail of the vacuum chamber (manufactured by Kurt J. Lesker Company). The chamber has an ISO-250 flange for a lid, CF-6" flange at the base, and seven NW-40 flange ports for vacuum feedthroughs and to connect to a turbomolecular pump. Detail B: Magnified view of the stainless steel top of the can, which shows the OFHC copper pin for heat sinking inside the probe head, four Swageloks for feeding the coaxial cables through to vacuum, and the three stainless steel tubes. A grease seal with a 10° taper mates the brass vacuum can to the stainless steel top of the can. Right: Image of the MRFM probe body mounted in the microscope superstructure.

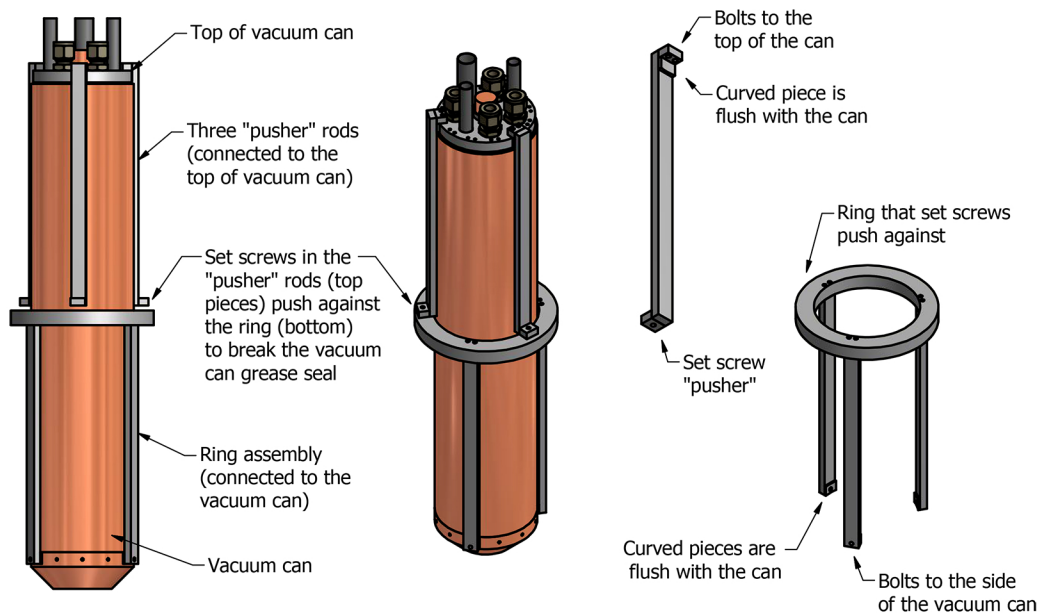


Figure 6.6: Schematics of the assembly used to dismantle the vacuum can. Left: Side-on view of the vacuum can with the assembly attached. The assembly consists of three “pusher” rods connected to the top of the can and a ring assembly with three rods connected to the base of the can. Set screws insert into the pusher rods to push against the ring and release the vacuum seal. Note that the can releases suddenly, so it is critical to support the can from the bottom during disassembly. Center: Angled view of the removal assembly. Right: Angled views of the pusher rod (top) and ring assembly (bottom).

suddenly.

In addition to the three vacuum tubes, a copper pin and four stainless steel ultra-torr vacuum fittings purchased from Swagelok (part SS-600-1-6WBT) also were welded (tubes and Swageloks) or soldered (copper pin) to the top of the can. The 0.75” OD oxygen-free high thermal conductivity (OFHC) copper pin is used to heat-sink the inside of the vacuum can to the liquid helium bath. The Swagelok fittings were designed to be combined with custom ferrules as vacuum feedthroughs for the coaxial cables. By feeding the coaxial cables through to vacuum at the top of the can, instead of with the fiber optic cables and electrical wires at the top of the probe, the heat-generating cables can be directly cooled in the liquid helium bath. The custom ferrules are discussed further in Section 6.3.2.

6.3.2 Vacuum Feedthroughs

Electrical wires and fiber optic cables were fed into vacuum *via* attachments to NW-40 ports on the MRFM probe vacuum chamber. Electrical wires were passed through standard, hermetically sealed 19-pin (Detorionics part DTIH-14-19PN) and 26-pin connectors (Detorionics part DTIH-16-26PN). Each connector was soldered with silver solder to the center of a blank NW-40 flange. Note that it was critical to slowly and uniformly heat the connectors prior to soldering in order to not crack the hermetic seals. The connectors were heated in an oven until they reached the temperature needed to make the solder connection (approximately 400°C). Fiber optic cables were used to watch the cantilever and the three dimensions of motion of the stage. Four 15 m lengths of 9/125 single mode fiber optic cable, purchased from Metrotek under the name “900 micron single mode” fiber with one end bare and the other end connectorized with an FC/APC connector, were fed into vacuum using 0.25” Ultra-Torr Swageloks (part SS-4-UT-A-4) fitted with custom teflon ferrules. A hole in the center of each teflon ferrule was drilled with a #67 drill bit (0.032” \approx 813 μ m) [158], and a light film of Apiezon N grease was applied inside the hole and around the surfaces of the teflon ferrule that mated with the Swagelok. Two Swageloks were welded to each NW-40 flange, totaling two flanges needed for the fiber feedthroughs.

New feedthrough methods for the coaxial cables were pursued with this probe design. Coaxial cables supply the transverse magnetic field at microwave (for electron spins) or radiowave (for nuclear spins) frequencies that is necessary to manipulate the sample spins in MRFM experiments. In the previous-generation probe, a single coaxial cable was fed through to vacuum at the top of the probe using a hermetically sealed SMA coaxial connector. 50 Ω impedance was maintained by terminating the line inside the probe head, which caused significant heating and raised the sample temperature from 4.2 K to often above 12 K when approximately 100 mW of microwaves were passed into the coaxial cable. For the third-

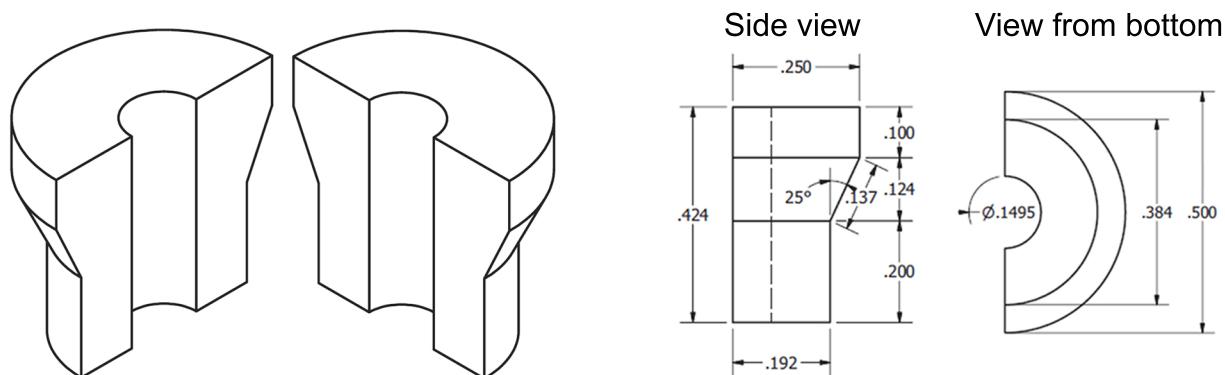


Figure 6.7: Schematics detailing the split ferrule used to feed a coaxial cable from liquid helium into vacuum. Left: Each split ferrule consisted of two identical aluminum halves. Right: Side and bottom-up schematics that indicate the dimensions of one of the split ferrule halves. Note that the provided measurements only should be used as a guide; dimensions should be adjusted based on the precise diameter of the coaxial cable and the dimensions of the obtained Swagelok. For example, the core of the ferrule should be bored to a radius equal to that of the coaxial cable, and the taper on the OD of the ferrule should mate flush with the taper of the Swagelok. To obtain liquid-helium-tight seals in initial tests (see text), strips of indium wire were pressed (1) along the inside width of each of the split ferrule halves (with the coaxial cable inserted between the two indium strips) and (2) around the perimeter of the split ferrule at the base of the taper. The split ferrule was inserted into a Swagelok to crush the indium.

generation probe, two design changes were made to mitigate microwave heating effects. Two sets of coaxial cables (four total cables) were designed to be fed into the probe, one set for microwaves up to 20 GHz and one set for radiowaves; the separate lines for microwaves and radiowaves have been installed for upcoming DNP experiments, as discussed in Section 6.1. For each set, one cable supplies the microwaves/radiowaves, and the second cable passes the microwaves/radiowaves back out of the probe to be terminated elsewhere.

The second design change pursued for the coaxial cable feedthroughs was to provide superior heat sinking by feeding the cables through the liquid helium bath and passing them into vacuum at the top of the vacuum can. 0.375" Swagelok tube fittings (part SS-600-1-6WBT) were purchased and welded to the top of the vacuum can (Figure 6.5, Detail B); the inner diameter of the Swageloks was wide enough to pass through preconnectorized cables.

Resealable, custom aluminum split ferrules were designed to fit around the coaxial cable (Figure 6.7). To seal each ferrule — which requires liquid-helium-tight seals between the coaxial cable and the ferrule, between the halves of the split ferrule, and around the outside of the ferrule — the use of indium wire (1.0 mm or 1.5 mm diameter; Alfa Aesar) or teflon tape was considered. Although a single split ferrule with a coaxial cable wrapped in indium wire successfully held vacuum both at room temperature and in liquid helium in a test setup (a long stainless steel rod with a single Swagelok at the base and an NW-40 vacuum fitting at the top), the split ferrules did not hold vacuum even at room temperature in the MRFM probe. The reason for this disappointing performance is unclear, but it is believed that the configuration of the top of the can, which has seven separate components in very close proximity, does not provide the clearance needed for sufficient tightening of the Swageloks. The probe has held vacuum at room temperature and in liquid helium by wrapping solid aluminum ferrules (the same design as the split ferrules, but one piece with no hole in the center) with 10 layers of teflon tape. Subsequent trials will involve switching to stainless steel ferrules to match the thermal contraction of the stainless steel Swageloks and coaxial cables, working to better match the taper between the Swageloks and the ferrules, and sealing the coaxial-filled split ferrules with an epoxy that can be thermally cycled, such as Stycast (Lake Shore Cryotronics, Inc.).

6.3.3 Mitigating Blackbody Radiation

Baffles were used to mitigate thermal losses due to blackbody radiation from the liquid helium reservoir to the close-to-room-temperature flange at the top of the dewar [157]. AMI recommended a 1/16" radial clearance between the 4.0" diameter neck of the dewar and the outer diameter of the baffles, meaning that the baffles should have a diameter of no more than 3.875". Because the bellows (located between the probe plate and the dewar top

hat) was made narrower than specification, and because the baffles must clear the bellows to assemble/diassemble the probe, the outer diameter of the baffles was further reduced to 3.8125". Six 1/16" thick copper baffles were installed along the stainless steel vacuum tubes between the probe plate and the top of the vacuum can. The baffles were clamped into place using two-piece clamp-on aluminum shaft collars with a 7/16" bore (McMaster-Carr, part 6436K134). Eight evenly-spaced half-baffles were also designed to feed down each of the three thin-walled stainless steel vacuum tubes to further mitigate the effects of blackbody radiation.

6.4 Third-Generation MRFM Probe Head

6.4.1 Probe Head Design

A schematic of the probe head, which consists of all of the microscope components inside of the vacuum can, is shown in Figure 6.8. The probe head houses the cantilever, the sample mounted on a coplanar waveguide that supplies the transverse magnetic field, and the three-dimensional stage. The cantilever motion is monitored using Fabry-Perot fiber-optic interferometers operating at 1310 nm [97, 159]. Three additional fiber optic cables were positioned to watch the motion of the three axes of the stage. Two OFHC copper plates were installed for heat-sinking. Currently copper posts connect the two copper plates; the posts will eventually be replaced by damped springs. Flexible coaxial cables were coiled between the top and bottom copper plates to supply the transverse field without disrupting the damping effects of the springs when installed. The sample and coplanar waveguide platform is bolted to the underside of the bottom copper plate. The cantilever is mounted on the three-dimension Pan-walker stage; the cantilever points up towards the sample. A rigid-

sample, moving-cantilever configuration was chosen so that the relatively-inflexible coaxial cables could be fed directly to the coplanar waveguide under the sample. The Pan-walker stage has 1 mm of coarse motion in each dimension and contains a piezoceramic tube for fine, nanometer-scale motion over a range of a few micrometers.

6.4.2 Heat Sinking of the Probe Head

Some of the features of the probe head that are used for heat sinking can be seen in Figure 6.8. As stated above, two OFHC copper plates were installed to heat-sink the probe head. A copper pin threaded against the top copper plate extends outside of the vacuum can to couple to the liquid helium bath. Glass beads (Delta electronics, part 41-10046-01-AU) were used to heat sink the center line of the coaxial cables on the top copper plate; the outer ground lines of the coaxial cables were passed through the liquid helium bath to be cooled to 4 K. To reduce the heat load passed from the room-temperature coaxial line to the low-temperature liquid helium bath and probe head, coaxial cable with a stainless steel outer shielding jacket was installed down the length of the probe body (AstroLab astro-cobra-flex cable, part 31000S-29043-29043-41.5). A stainless steel jacket incurs slightly higher microwave transmission losses than regular coaxial cable, but also exhibits lower thermal transmission. Before entering the probe head, the coaxial cable was transitioned to a cable with a standard tin-plated copper shielding jacket (RF COAX Inc. RF cable assembly part S086MM-47R, 0.086" OD tin-plated copper semi-rigid cable with SMA male to SMA male connectors rated for use up to 27 GHz).

Copper foil was used to heat sink critical components of the probe to the copper plates. Only one piece of copper foil, which is located between the bottom copper plate and the cantilever mount, was installed when the images in Figure 6.8 were collected. The copper foil is 0.001" thick (99.999% metals basis; Alfa Aesar, part 10950) and was cut into approximately

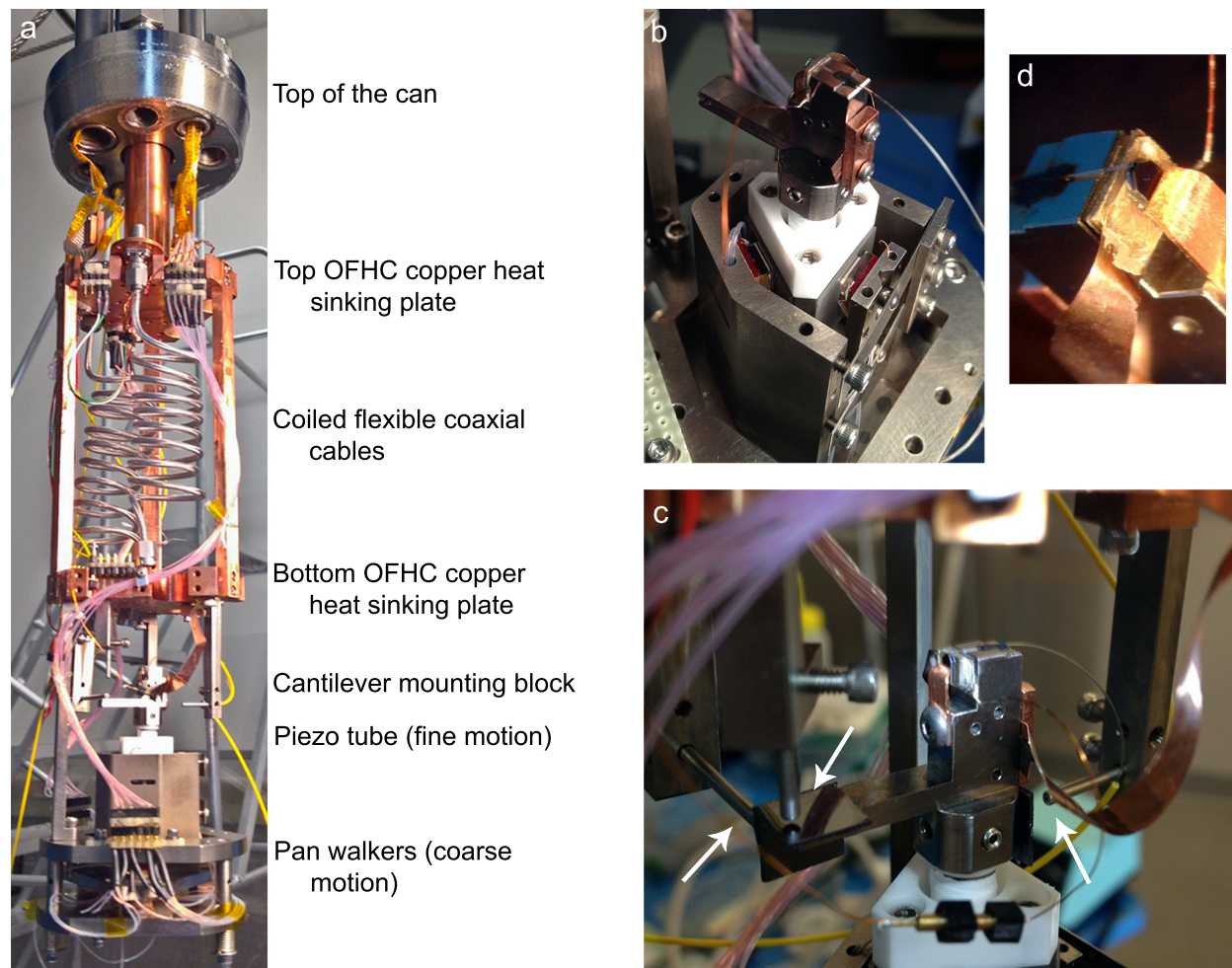


Figure 6.8: Images of the third-generation MRFM probe head. (a) Image of the full length of the probe head. The copper pin soldered to the outside of the top of the can passes into the probe head and heat sinks the top and bottom copper plates. Coaxial cables inserted from the top of the can (not shown) are heat-sunk to the top copper plate using glass beads and routed *via* coiled flexible coaxial cables to the sample platform bolted to the underside of the bottom heat-sinking plate (not shown). The cantilever is mounted on a piezo tube contained within a three-dimensional custom-built Pan-style nanopositioner. The fine-motion piezo tube achieves $2\ \mu\text{m}$ motion in each direction at $4.2\ \text{K}$; the Pan-style walkers are used for coarse motion and have a range of $1\ \text{mm}$ in x , y , and z . (b) Magnified, angled view of the Pan z -walker prism (white triangle) housed in its titanium casing. (c) Magnified view of the cantilever mount and the three fiber optic cables (encased in stainless steel sheaths) which are used to watch the motion of the stage. The fibers, which are pointed at three silicon mirrors, are highlighted by the white arrows. (d) Further magnified view of the fiber optic cable watching the cantilever motion. The fiber is glued to the cantilever mounting block (black Stycast epoxy, left-hand side of the frame), and the cantilever paddle is positioned so that the paddle is directly over the core of the fiber. The cantilever handle die (silicon chip in the center of the frame) is mounted on a drive piezo and is held in place with a copper clip.

1 mm wide strips. Very thin foil was used to minimize the propagation of vibrations to the cantilever and sample. In order to improve the thermal conductivity, the copper foil was annealed for 3 hours at 600-650°C in forming gas with 95% argon and 5% hydrogen. Note that the foil should not be touched with metal tweezers or scissors prior to the anneal to avoid contamination. The annealing was conducted at the Army Research Laboratory by Doran Smith's group; Smith *et al.* have measured the thermal conductivity of this type of foil to be in line with what is expected for 99.999% pure copper [160]. Before the copper foil was bolted in place, a thin film of Apiezon N grease was applied to the ends of the foil to enhance thermal conductance at cryogenic temperatures [161].

6.4.3 Hang-Down Geometry

There are two commonly-used experimental geometries for MRFM experiments. For the third-generation microscope, the hang-down geometry [53], in which the length of the cantilever is parallel to the external field, was chosen over the SPAM (Springiness Preservation *via* Aligning Magnetization) geometry [139], where the width of the cantilever is parallel to the external field. Schematics of both geometries are shown in Figure 6.9. In the SPAM geometry there is no observed field-damping of the magnetic tip [30, 55, 162]. Magnetic damping has been observed in the hang-down geometry [56, 93] for micrometer-diameter magnetic particles; however, magnetic damping is not expected to be an issue for small nanomagnets.

MRFM signal is significantly increased by working in the hang-down geometry; the relative magnetic field gradient is three times larger in the hang-down geometry than in the SPAM geometry [163]. Additionally, *in situ* magnetic tip characterization using frequency-shift cantilever magnetometry (Sections 4.1 and 4.4) can only be conducted in the hang-down geometry [58, 82].

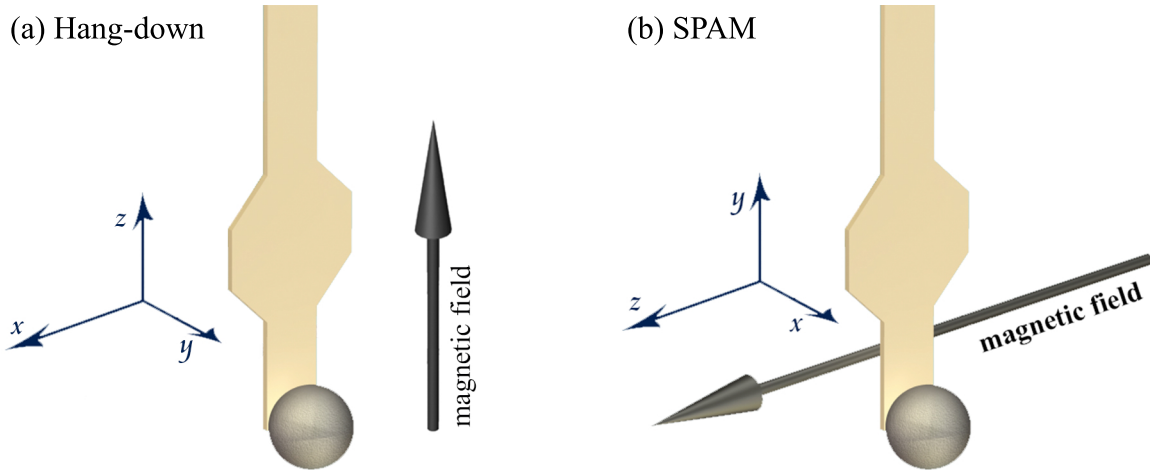


Figure 6.9: Schematics of the hang-down and SPAM geometries used in MRFM experiments. (a) The hang-down geometry, in which the applied magnetic field is parallel to the length of the cantilever, has been chosen for the third-generation MRFM microscope. (b) The SPAM geometry, in which the magnetic field is instead parallel to the width of the cantilever, was used in the previous-generation microscope.

Cantilever damping was assessed as a function of applied magnetic field for an attonewton-sensitivity cantilever with an integrated $4\ \mu\text{m}$ diameter (nominally spherical) nickel magnetic particle (Novamet, CNS-10). The data shown in Figure 6.10 were collected at $T = 4.2\ \text{K}$ for a cantilever with a spring constant $k_c = 1\ \text{mN m}^{-1}$. The dissipation $\Gamma = k_c / (2\pi f Q)$ and minimum detectable force $F_{\text{min}} = \sqrt{4k_B T \Gamma}$ were determined. At zero field, $\Gamma = 1.2 \times 10^{-12}\ \text{Ns/m}$ and $F_{\text{min}} = 17\ \text{aN}$. At a field of $0.6\ \text{T}$, which is the approximate field used in electron spin resonance (ESR) MRFM experiments, $\Gamma = 6.3 \times 10^{-12}\ \text{Ns/m}$ and $F_{\text{min}} = 38\ \text{aN}$. These results indicate that by working in the hang-down geometry, the dissipation experienced by the nominally spherical $4\ \mu\text{m}$ magnet-tipped cantilever at high applied magnetic field is increased by a factor of five. However, the SNR for this experimental setup should still be sufficient to conduct ESR measurements using the spin detection protocol in Ref. 30.

A new spin detection protocol COZMIC has been successfully used with nanomagnet-tipped cantilevers in the hang-down geometry for a nuclear magnetic resonance MRFM experiment. This protocol was introduced in Ref. 58 and is discussed in Section 5.2.4.

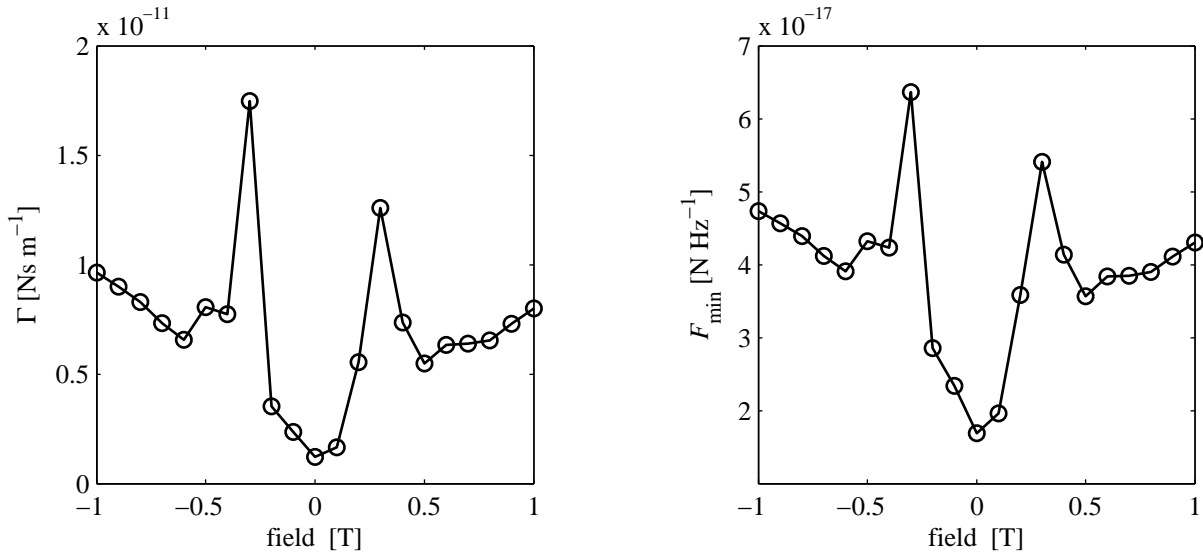


Figure 6.10: Magnetic damping in the hang-down MRFM geometry as a function of applied magnetic field for a 4 μm nickel magnet attached to an attonewton-sensitivity silicon cantilever. Dissipation Γ and the minimum detectable force F_{\min} were calculated for a temperature $T = 4.2$ K and a cantilever spring constant of $k_c = 1$ mN m^{-1} .

6.4.4 Pan-Walker Stage with Three-Dimensional Motion

Three-dimensional motion was achieved using a custom-built Pan-style nanopositioner (Figure 6.8(a-b)) [164–166], which is known to maintain performance at cryogenic temperatures and, due to its rigid design, is less susceptible to excitation by ambient vibrations than commercial Attocube positioners. Due to slow and steady stepping, the Pan-walker stage moves without any backlash, in contrast with commercial slip-stick positioners. The Pan-walker stage allows more than 1 mm of coarse motion in each x , y , and z direction. A piezo tube was positioned inside the core of the Pan walker to enable nanometer-precision motion over a 2 μm range in each direction. The piezo tube, which was custom-manufactured by EBL Products Inc. (made from material EBL #3), had a 0.250" outer diameter, a 0.190" inner diameter, and was 1.850" long. The tube contained four 90° quadrants, was grounded in the center, and had gold electrodes on the outer diameter. No gold was coated on the final 0.1" of the piezo tube at each end so that parts that were glued to the piezo tube were

not exposed to high voltages. The cantilever mount (Figure 6.8(c-d)) — which holds the cantilever, a drive piezo to excite cantilever motion, and a fiber optic cable to watch the cantilever motion — was mounted to the top of the piezo tube.

The Pan-walker stage was fabricated primarily from titanium and consisted of two parts: a prism for z -motion (see Figure 6.8(b)) and a plate for motion in the x and y directions (see Figure 6.8(a)). Low-friction sapphire plates were glued using Stycast epoxy to the surfaces of the z -walker prism and the x - y plate. Each shear piezo stack was comprised of two shear piezos that were glued together with silver paste to increase the range of motion. The piezoceramic plates with shear polarization were custom-fabricated by EBL Products Inc. (made from material EBL #4). They had an area of $0.275'' \times 0.275''$, and were $0.050''$ thick. One corner of each piezo was removed ($0.07'' \times 0.07''$) to facilitate adhesion of electrical wires to the gold electrodes on the piezos. The piezos were glued with silver paste to the outer frame of the walker, and alumina plates were adhered with Torr Seal epoxy to the side of the piezo pressed against the sapphire sheets. The alumina-sapphire interface has relatively low friction, so the alumina sheets glide across the sapphire plates when moved slowly. A schematic of one piezo stack is shown on the right-hand side of Figure 6.11.

Six shear piezo stacks were used for each direction of motion of the Pan-walker stage. The stepping mechanism is illustrated on the left-hand side of Figure 6.11. The x and y piezo stacks were glued together; three stacks were positioned under the x - y stage plate, and the other three stacks were placed at the same positions above the plate. The tension to the x and y piezos was set by adjusting the force of three springs on a tensioning plate located underneath the bottom set of x - y piezos. Three pairs of z piezo stacks move the z -prism; two piezo stacks are located on each of the three triangular surfaces of the z -stage. Tension to the z stage is supplied by tensioning a beryllium copper leaf spring on the front face of the z stage; a sapphire ball bearing transfers the tension to the stage.

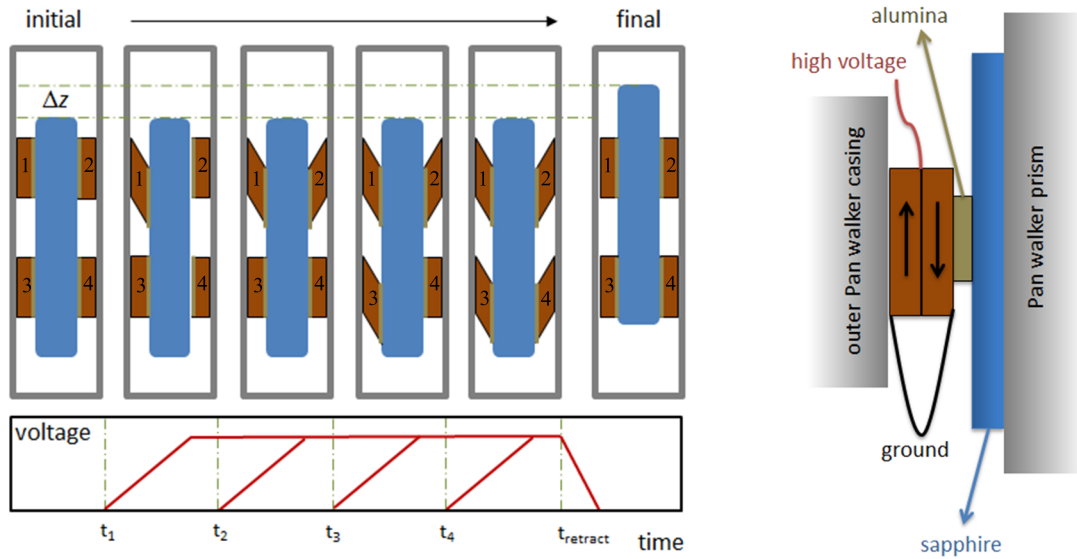


Figure 6.11: The stepping mechanism of the z -prism of the Pan-style nanopositioner. The mechanism for the motion of the x - y stage is almost identical. Left: Cartoon of how shear piezos (brown) are used to step the central prism (blue) of the third-generation MRFM probe head Pan-walker stage. For simplicity only four of the six piezo stacks are displayed. In the initial state, the central prism is held by all the piezo stacks. At time t_1 , piezo stack 1 is charged and shears. Since the prism is still held by the other three piezos, it does not move. One-by-one the other piezo stacks are charged and shear. At time t_{retract} , the charges on all the piezo stacks are simultaneously dropped, and the prism is pushed forward a distance Δz in one smooth step. Right: Detailed schematic of one piezo stack between the central prism and the titanium outer casing. Each piezo stack is comprised of two shear piezos that move in opposite directions (as indicated by the arrows) to increase the range of motion. The high voltage sides of both piezos are in the center, and the outsides are grounded. The piezo stack was glued to the outer Pan-walker stage casing and to an alumina sheet. A sapphire plate was glued to the surface of the z -walker prism. Motion occurs along the alumina-sapphire interface.

6.4.5 Coplanar Waveguides

In MRFM experiments, a transverse magnetic field B_1 is necessary is used to saturate nearby sample spins. We have studied the strength of transverse fields generated using multiple types of transmission lines. Microstripline halfwave resonators have been used to generate modest fields of 3.9 mG, with 100 mW passed into the top of the second generation probe [30]. Recently, two coplanar waveguide designs have been considered to increase the B_1 field strength. Both types of waveguides were lithographically patterned on ultra-high-resistivity silicon substrates (purchased from University Wafer, intrinsic silicon with resistivity $> 20,000 \Omega \text{ cm}$, dielectric constant $\epsilon_r = 11.7$, $\langle 100 \rangle$ oriented, 100 mm diameter, 500 μm thick, single side polished).

In the first design, coplanar waveguides with finite-width ground planes were fabricated [61]. The waveguides had a 321 μm wide middle conductive line and two 342 μm wide outer conductive lines that were separated by 290 μm wide interline gaps [158] to achieve 50 Ω impedance. In order to avoid problems associated with standing waves arising from imperfect termination, the waveguides were designed with a short at one end. In MRFM experiments, the cantilever approached the sample surface above the middle of one of the shorted segments. The short that terminated the three conductive lines was 300 μm wide. All of the conductive lines were made by patterning 100 nm thick gold on top of a 5 nm titanium adhesion layer. To pass microwave frequencies in to the center line of the waveguide, the waveguide silicon chips were inserted into high-dielectric-constant circuit boards equipped with end launch SMA connectors. The gap between the circuit board and the chip was designed to fit snugly and had a gap of less than 0.5 mm on all sides. The conductive lines were connected between the circuit board and the silicon chip by using three gold wire bonds per conductive line. The waveguide board was made of 0.015" thick Arlon ($\epsilon_r = 10.0$), with 1 oz/ft² copper cladding with a soft gold finish on the front side of the board [158]. The

board was patterned to match the dimensions of the center line and gaps in the waveguide silicon chips. From measurements of the mechanically-detected ESR signal versus power in the second generation probe, the coil constant at the short of the coplanar waveguide was estimated to be $45 \text{ mG W}^{-1/2}$, with the power measured for convenience at the input to the probe. At a typical power into the probe head of $P_1 = 15 \text{ dBm} = 32 \text{ mW}$, the rotating frame microwave field amplitude at the sample was estimated to be $B_1 \approx 8 \text{ mG}$. This is a factor of two improvement over the field strength in Ref. 30.

Most recently, coplanar waveguides with infinite ground planes have been prepared. The large-area ground planes ensure a better connection to the ground. These waveguides were fabricated on silicon chips that are 9.8 mm long and 4.75 mm wide. They had a 1016 μm wide middle conductive line and two outer conductive lines that extended to the edges of the chip. To achieve a 50Ω impedance, the interline gaps between the center line and the ground planes were 432 μm . The conductive lines were comprised of a 5 nm titanium adhesion layer (deposited at a rate of 1.67 $\text{\AA}/\text{sec}$), approximately 800 nm of copper (5.56 $\text{\AA}/\text{sec}$), and a 30 nm thick gold top layer for wire bonding (0.8 $\text{\AA}/\text{sec}$). The titanium and copper layers were deposited by sputtering (AJA sputtering tool), and the gold was subsequently deposited by thermal evaporation (CVC SC4500 Evaporation System). The chips were again designed to insert into square gaps in the center of circuit boards with a high dielectric constant and to be electrically connected using gold wire bonds. This generation of circuit boards was made of 0.1" thick TMM10i ($\epsilon_r = 9.8$; purchased from PCBFabExpress). It was anticipated that the low B_1 generated by the previous coplanar waveguide design may have been due in part to the field lines being pulled down toward the copper sample mounting block below the thin Arlon boards, which would act as a ground plane. The significantly thicker TMM10i boards used here are expected to provide a thicker buffer layer of high-dielectric-constant material and push more of the field into the sample above the coplanar waveguide. The TMM10i boards were again coated with 1 oz/ft² copper cladding with a soft gold finish that

was patterned to match the design of the silicon chip. The field generated from these new chips will be tested in upcoming MRFM experiments in the third-generation MRFM probe.

6.5 Discussion

When fully operational, the third-generation magnetic resonance force microscope will have three-dimensional scanning capabilities with nanometer-scale precision over a 2 μm fine scanning range and coarse motion up to 1 mm in each direction. The microscope has been designed for the cantilever to be positioned on the nanopositioner stage, which leaves the rigid, large-area transmission line substrate free to accept a wide range of as-fabricated samples and devices. Enhanced vibration isolation has been achieved by designing a new microscope superstructure with a floating, lead-filled top plate. Better heat-sinking has been implemented to improve temperature stability within the probe, and a new bottom-loading dewar was introduced to improve the liquid helium hold time. At the time of writing, the probe has been cold tested and vacuum tested, and magnet operation and hold time have been verified. The Pan-walker stage has been tested at room temperature and is being optimized for operation at liquid helium temperatures.

The new microscope will enable many new and exciting MRFM experiments. Three-dimensional motion will be possible for the first time in our laboratory, which is essential for three-dimensional imaging and is needed in order to use either high-sensitivity microwires for NMR-MRFM experiments [60] or microscale versions of the coplanar waveguides for high-sensitivity ESR-MRFM measurements. In Chapter 5, methods were discussed for the fabrication of high-gradient cobalt nanomagnet-tipped cantilevers and their use to detect nuclear magnetic resonance with better than 500 proton magnetic moment sensitivity demonstrated. For a tip-sample separation of 13.1 nm and under the signal averaging conditions of Ref. 12,

this sensitivity corresponds to a proton imaging resolution of 5 to 10 nm in each dimension. These nanomagnet-tipped cantilevers are ready to be used in the third-generation MRFM microscope as soon as the optimization of the three-dimensional stage for operation at liquid helium temperatures is completed. It also may be possible to further enhance the resolution of NMR-MRFM experiments using DNP; however, definitive studies of DNP in an MRFM experiment have not yet been conducted by any MRFM group because no microscope exists with the ability to simultaneously apply both microwaves and radiowaves. We believe that the third generation Cornell MRFM microscope described in this chapter will be the first microscope capable of these double resonance experiments. When fully operational, we expect the microscope to be used to investigate the mechanism of DNP in the high magnetic field gradients experienced by spins close to nanomagnet tips [167], as well as to explore enhancements of SNR in NMR-MRFM experiments by using DNP to polarize nuclear spins.

Acknowledgements

The development of this microscope has been a joint effort over a two-year period, and I am grateful for the contributions of many collaborators. I thank my colleagues Eric Moore and Lei Chen for co-developing the microscope; Eric collaborated with me on the design of the microscope superstructure, and the probe head was largely designed by Lei. I also thank Eric for collecting the vibrational data in the Baker and PSB laboratories, and Lei and Christine Gleave both for collecting the MRFM data on the magnetic damping of a large magnetic tip in the hang-down MRFM geometry and for supplying information on the fabrication methods for our coplanar waveguides. Daniel Rugar and John Mamin at the IBM Almaden Research Center and Doran Smith at the Army Research Laboratory provided invaluable advice on microscope design during laboratory tours. Thanks to Doran also for annealing the copper foil and for giving a wealth of advice on heat sinking and overall probe construction.

Raffi Budakian and John Nichol at University of Illinois at Urbana-Champaign graciously shared their unpublished Pan-walker designs. Seamus Davis, Tien-Ming Chuang, and Milan Allan at Cornell University shared their STM superstructure CAD and provided excellent advice for maximizing vibrational isolation. Thanks to Lee Harrell at the West Point Military Academy for helpful discussions on the hybrid hoist system. Thanks to Cornell's Research Services Shop, and particularly Jason Russell and Daniel Sheerer, for assistance with redesigning PSB B19. And special thanks goes to the Cornell Laboratory of Atomic and Solid State Physics Machine Shop, especially Rodney Bowman, Chris Cowulich, and Jeffrey Koski, for fabricating the probe, collaborating on design adjustments, and for countless helpful conversations. Work in this chapter was conducted with the financial support of the National Institutes of Health (Grant No. 5R01GM-070012), the Army Research Office MultiUniversity Research Initiative (Grant No. W911NF-05-1-0403), and the National Science Foundation through the Cornell Center for Nanoscale Systems (Grant Nos. EEC-0117770 and EEC-0646547). This work was performed in part at the Cornell NanoScale Facility, a member of the National Nanotechnology Infrastructure Network, which is supported by the National Science Foundation (Grant No. ECS-0335765). Wire bonding was accomplished using resources available in the Cornell Center for Materials Research, which is supported by the National Science Foundation Materials Research Science and Engineering Centers program (Grant No. DMR-0520404).

CHAPTER 7

OVERALL CONCLUSIONS AND OUTLOOKS FOR THE NEXT GENERATION OF CORNELL MRFM FABRICATION

In the work presented in this thesis, the critical need within the magnetic resonance force microscopy community for the development of a fabrication protocol to prepare high-gradient nanomagnets on cantilevers has been achieved. The primary objective of this work was to fabricate overhanging nanomagnet-tipped cantilevers with sufficiently large magnetic field gradients to conduct high-resolution MRFM imaging experiments.

To reach this goal, a new magnet-on-cantilever fabrication protocol was developed that decoupled the preparation of the nanomagnets from the fabrication of attonewton-sensitivity cantilevers. Nanomagnets were batch-fabricated on suspended silicon micrometer-scale chips and were attached to separately-fabricated cantilevers using focused ion beam manipulation. Using this new approach, nanomagnets were not exposed to high-temperature processing steps and could be patterned using the non-damage-inducing techniques of electron beam lithography and electron beam evaporation. These advantages allowed for the high-yield fabrication of both robust nickel nanomagnets and temperature-susceptible cobalt nanomagnets. The magnet-tipped chip process required only a few days of processing time, which facilitated rapid optimization of processing conditions. Additionally, both spectroscopic and microscopic analysis of as-deposited nanomagnets were possible for the first time. Cantilever magnetometry indicated that cobalt nanomagnets exhibited saturation magnetizations consistent with the theoretical value for fully-saturated cobalt. Characterization of similarly-processed cobalt magnetic films using X-ray photoelectron spectroscopy (XPS) with depth profiling indicated that unprotected cobalt films incurred less than 10 nm of oxidation damage, and that oxygen contamination was prevented by capping the cobalt layer with 10 nm of platinum.

A cobalt magnet-tipped cantilever fabricated using the new magnet-tipped chip protocol was successfully used to detect spin variance signal from protons in a polystyrene film with better than 500 proton magnetic moment sensitivity in a 1 Hz detection bandwidth. The observed vertical tip-field gradient of 4.4 to 5.4 MT m^{-1} is comparable to the 4.2 MT m^{-1} field gradient produced by the $\text{Fe}_{70}\text{Co}_{30}$ pillar in the sample-on-cantilever experiment of Ref. 12 that achieved 4 to 10 nm resolution MRFM imaging. Moreover, this gradient is 8 to 10 times larger than the best tip gradient demonstrated previously in a magnet-on-cantilever MRFM experiment [53].

That such a large gradient has been achieved in a magnet-on-cantilever MRFM experiment is an exciting advance. The tip-field gradient produced by these cobalt nanomagnets has been calculated to be sufficient to detect single electron spins by ESR-MRFM with only a few minutes of signal averaging per point, which would enable three-dimensional mapping of the positions of multiple nitroxide spin radicals on uniformly-labeled proteins to determine their tertiary structure [30]. The field gradients produced by the cobalt-tipped cantilevers also are large enough to enable the characterization of as-fabricated semiconductor devices where, for example, Stark shifts of magnetic resonance transitions [45, 168, 169] allow the measurement of internal electric fields in semiconductor devices containing quadrupolar nuclei [47, 170, 171]. Additionally, moving the sample off-cantilever is anticipated to allow the full battery of cryoelectron microscopy (cryo-EM) sample preparation techniques [49, 50] to be applied in an MRFM experiment to prepare fragile biomolecules, macromolecular complexes, and thin sections of biological material. In contrast with cryo-EM, MRFM can accommodate micrometer-thick samples, and image contrast can be achieved by isotopic labeling, which is non-perturbative. MRFM's present resolution of 4 to 10 nm is competitive with what has been demonstrated in electron cryo-tomography (cryo-ET) studies of subcellular structures [11], organelles [172], neuronal synapses [9], and viral synapses [10] where studying a single copy of the structure is essential. When multiple precisely identical copies of

a highly symmetric and large macromolecule or macromolecular complex are available, cryo-EM with single particle analysis can achieve near-atomic resolution. Frustratingly, broad classes of trafficking agents such as exosomes [23] and membrane proteins remain difficult to study by cryo-EM because the associated macromolecules or macromolecular complexes are disordered, have molecular weights less than 100 kDa [24], or simply do not retain their native structure in aqueous solution. With only slightly improved resolution, we anticipate that the type of magnet-on-tip magnetic resonance force microscope demonstrated here can begin to contribute to understanding such important biological nanostructures.

To continue to improve sensitivity in MRFM experiments, it will be critical to reduce the nanomagnet leading edge damage layer. Simulations based on the experimental MRFM data presented in Chapter 5 indicated that if all nanomagnet damage is localized at the magnet leading edge, there could be up to 51 nm of leading edge damage. These simulation results contrast with the less than 10 nm of damage estimated using XPS with depth profiling. It is expected that the damage to the cobalt nanomagnet studied in Chapter 5 was due to a combination of oxidation of all unprotected cobalt surfaces to a depth of 10 nm, surface roughness on the magnet leading edge, roughness of the sample surface, and a protrusion of the titanium underlayer past the cobalt leading edge. To decrease the spacing between the magnetic material in the nanomagnet and the sample surface — and thus increase the achievable tip-field gradient — it will be essential to determine the precise extent and sources of leading edge damage of individual nanomagnets in future experiments.

Characterization techniques are available to assess elemental degradation of nanoscale magnetic particles. The use of scanning transmission electron microscopy (STEM) and electron energy loss spectroscopy (EELS) to visualize and determine the elemental composition of the nanomagnets with nanometer-scale resolution was demonstrated in Chapter 2. STEM could be used in future work to determine the extent of leading-edge roughness and assess

whether titanium extended past the leading edge of the magnetic material. EELS is capable of obtaining side-on or top-down two-dimensional maps of the elemental composition of the nanomagnets. Energy-dispersive X-ray spectroscopy (EDS) could rapidly determine contaminant surface elements of sub-100 nm wide nanomagnets [91]. Additionally, Auger electron spectroscopy combined with depth profiling could be used to reconstruct a full three-dimensional map of the elemental composition of a nanomagnet with nanometer-scale resolution [173].

Once sources of damage contributing to increased tip-sample separation are understood, the magnet-tipped chip fabrication protocol can be improved to maximize the magnetization at the nanomagnet leading edge. Surface roughness of the nanomagnet could be reduced by depositing the magnetic material at a faster rate to decrease the grain size [174]. If damage is attributed to oxidation, the introduction of barrier layers could be reconsidered. A capping layer coating the leading edge side wall of the nanomagnet could be used to protect the nanomagnet leading edge against oxidation or other degradation of the magnetic material. Since the nanomagnets are fabricated off-cantilever, protective encasement layer processing does not need to be compatible with the constraints of cantilever processing; the magnet-tipped chips could be fully coated with the films used to encase the nanomagnets, as long as the protective layers only extend 2-5 nm past the leading edge of the nanomagnet.

In order to avoid oxidation of the leading edge of the nanomagnet, the magnet side walls must be protected prior to exposure to an atmospheric environment. The ideal process would involve electron beam evaporation of nanomagnets and ALD deposition of a capping layer material in tandem without breaking vacuum. However, the availability of such a system is not known. A potentially viable alternative would be to deposit magnetic material in a trench that is encased with a protective coating. A proposed protocol involves: (1) creating a nanomagnet-sized trench in an easily-etchable sacrificial material such as silicon dioxide

or silicon nitride; (2) coating the trench with a thin layer (2-5 nm thick) of an etch-resistant material that also acts as an oxidation barrier, possibly ALD tantalum oxide or a bilayer of an ALD alumina oxidation barrier with an etch-resistant ALD tantalum nitride outer shell; (3) conformally depositing the magnetic material inside the trench, likely using sputtering; (4) using chemical mechanical polishing (CMP) to remove the excess magnetic material on the wafer; and (5) etching the sacrificial material. This procedure could fabricate thinly-encased nanomagnets with leading edges that are fully protected against oxidation damage. Although a few nanometers of the unprotected top surface of the nanomagnets would oxidize, the thickness of magnetically inactive material at the nanomagnet leading edge would only be the 2-5 nm thick protective film. Thus, the leading-edge magnetically inactive layer could be reduced and the achievable tip-field gradient could be significantly improved. Extensive process development would be required to implement this protocol, including the fabrication of nanoscale trenches with highly vertical side walls and the employment of a CMP slurry that does not damage the magnetic material.

An alternative method to create a nanomagnet with limited leading edge damage would be to revisit the use of serial focused ion beam (FIB) milling to selectively remove the damaged portion of the nanomagnet leading edge. Fabricating the nanomagnets on magnet-tipped chips would be advantageous since the magnets could be rigidly fixed on the silicon chips during FIB milling. Conventional FIB milling causes damaging gallium ion implantation; however, new low-energy polishing techniques have been used with less than 2 nm of damage to the side wall [118]. Damage to the remainder of the nanomagnet could be minimized by protecting the top surface with platinum. FIB milling with alternative ion sources, such as helium, could also be considered [175]. Since helium ions are lighter than gallium ions, helium ions channel through some materials without disrupting the crystal structure or inducing damage; the extent of magnetization damage induced by helium ion beam (HIM) milling of polycrystalline nickel is not known and would need to be assessed, but the results

presented in Ref. 175 on high-resolution HIM milling of nickel are promising. Although this method would lead to device-to-device variations and would require additional processing time per nanomagnet, minimizing the nanomagnet leading edge damage layers using HIM milling could provide valuable proof-of-concept information about the upper bound for the achievable tip-field gradient.

In conclusion, the work in this thesis has significantly advanced the capabilities of magnet-on-cantilever MRFM and has positioned the field of MRFM to study exciting new classes of biological and materials-based samples. The newly-developed magnet-tipped chip protocol allows for the high-yield fabrication of high-gradient cobalt nanomagnets. It is projected that these cobalt nanomagnets can be used in magnet-on-cantilever MRFM experiments to detect single electron spins and achieve few-nanometer resolution imaging of nuclear spins. Additionally, the magnet-tipped chip protocol will enable rapid prototyping of new fabrication methods to protect nanomagnet side walls, minimize leading edge damage, and facilitate further enhancement of the magnetic tip-field gradient.

APPENDIX A

**PROTOCOL FOR THE FABRICATION OF NANOMAGNET-TIPPED
SILICON CHIPS**

In this Appendix, details are provided for the fabrication of nanomagnet-tipped chips. All work was conducted at the Cornell NanoScale Science and Technology Facility (CNF).

Soitec silicon-on-insulator (SOI) wafers (Soitec product number G4P-005-02) were used for fabricating the magnet-tipped chips. The wafers had a device silicon thickness of 340 nm, a buried oxide (BOX) thickness of 400 nm, and a silicon handle wafer thickness of 500 μm . The device silicon resistivity was 14 to 22 $\Omega\text{ cm}$, corresponding to a boron dopant concentration of 6 to $9 \times 10^{14}\text{ cm}^{-3}$.

Solvents were obtained from Fisher Scientific or J. T. Baker and used as received; all solvents met either ACS grade or electronic grade requirements. Electron beam (e-beam) lithography resists were supplied by Microchem. All metals were from Kurt J. Lesker Company. The crucibles of magnetic materials were stored separately from the common-access crucibles to ensure against contamination.

When spinning all e-beam resists, the ramp rate was 1000 rpm. All e-beam lithography steps were conducted using either a JEOL JBX-6300FS or JEOL JBX-9300FS 100 kV Electron Beam Lithography System. The systems could be used interchangeably, but alignment was most straight-forward if the same slot on the same tool was used consistently for a given wafer. On the JEOL 9300, a current of 2 nA was used. On the JEOL 6300, the fourth lens mode was used with a current of 1 nA. In the following sections, the names of the CAD files used on the CNF JEOL 6300 in the directory `\job\user\longenecker\201106_mag_chips` are listed; these files can be accessed by any CNF user and can be used as references for the creation of the appropriate files for alignment marks and the magnet-tipped chip layers.

Assessment of the yield of individual steps and the overall fabrication process was conducted using either the Zeiss Supra or Zeiss Ultra High Resolution Field Emission scanning electron microscopes with beam voltages of 2 kV or 5 kV.

A.1 Wafer Layout

Four sets of e-beam alignment marks were fabricated on each wafer; three sets were for the three aligned e-beam lithography layers of the magnet-tipped chip process, and the fourth set of alignment marks was spare. Each set of alignment marks consisted of both global and local marks. All alignment marks consisted of 100 nm of platinum, were “+”-shaped, and had a line width of 3 μm . Global marks, which were 2 mm long, were used to locate the center of the wafer and adjust the rotational alignment. Local marks, which were 60 μm long, were used to find the center of each die of magnet-tipped chips. An example of the wafer layout, including one set of global marks, blue squares to designate the magnet-tipped chip dies, and one set of local marks, is shown in Figure [A.1](#).

Global P and Q marks were centered vertically on the wafer and placed laterally on the far left and right sides. The sets of four global marks were spaced in a 2×2 grid with 2 mm separations in each direction. The P and Q marks were approximately 70 mm apart. Sets of local marks were set at the corners of each chip, totaling 16 local marks per set. The marks were spaced 8.0 mm, 7.5 mm, or 7.0 mm from the center of the die for the first, second, or third layers of the process, respectively. The four dies of magnet-tipped chips were arranged in a 2×2 grid centered with the center of the wafer and spaced apart from each other in x and y by 30 mm.

The precise locations of all marks are detailed in Table [A.1](#). Note that the positions are denoted based on the calibration sequence they are used with on the JEOL systems; the AGCRG locations are listed in the stage coordinate system, where the top-left corner

Calibration	Etch slit layer	Magnet layer	Etch pit layer	Extra layer
AGCRG (JEOL 9300) ^a	<i>x</i>	(A) 154; (B) 64	(A) 156; (B) 66	(A) 156; (B) 66
	<i>y</i>	(A) 64; (B) 174	(A) 64; (B) 174	(A) 66; (B) 176
AGCRG (JEOL 6300)	<i>x</i>	69,000	71,000	71,000
	<i>y</i>	84,000	84,000	86,000
SETWFR	<i>x</i>	stage - AGCRG <i>x</i>	stage - AGCRG <i>x</i>	stage - AGCRG <i>x</i>
	<i>y</i>	AGCRG <i>y</i> - stage	AGCRG <i>y</i> - stage	AGCRG <i>y</i> - stage
Material center offset	<i>x</i>	-36,000	-34,000	-34,000
	<i>y</i>	1,000	1,000	-1,000
<i>P</i> -point	<i>x</i>	36,000	34,000	34,000
	<i>y</i>	1,000	1,000	-1,000
<i>Q</i> -point	<i>x</i>	15,000	15,000	15,000
	<i>y</i>	15,000	15,000	15,000
CHIPAL	<i>x</i>	±8,000	±7,500	±6,500
	<i>y</i>			
Center	<i>x</i>			
	<i>y</i>			
Marks	<i>x</i>			
	<i>y</i>			

Table A.1: Positions of the e-beam lithography global and local alignment marks written during the alignment mark step and used for the subsequent aligned magnet-tipped chip fabrication layers. The numbers are organized based on the calibration sequence for which they are used. The AGCRG calibration, which sets the gain by measuring the *P*-point global mark, uses the stage coordinate system and thus has different values based on which slot in the JEOL 9300 or JEOL 6300 systems is used. The SETWFR calibration, which is used to set the center and rotation of the wafer, and the CHIPAL calibration, which is used to locate the local marks and find the center of each die, use the material coordinate system and are the same regardless of which tool or slot is used. Within the SETWFR calibration, the term “stage” refers to the stage position of the mark as viewed in the JEOL software and the terms “AGCRG *x*” and “AGCRG *y*” refer to the appropriate AGCRG values listed in the corresponding section of this table. All values have units of micrometers.

^aNumbers in these rows must be multiplied by 1000 when input into the tool software.

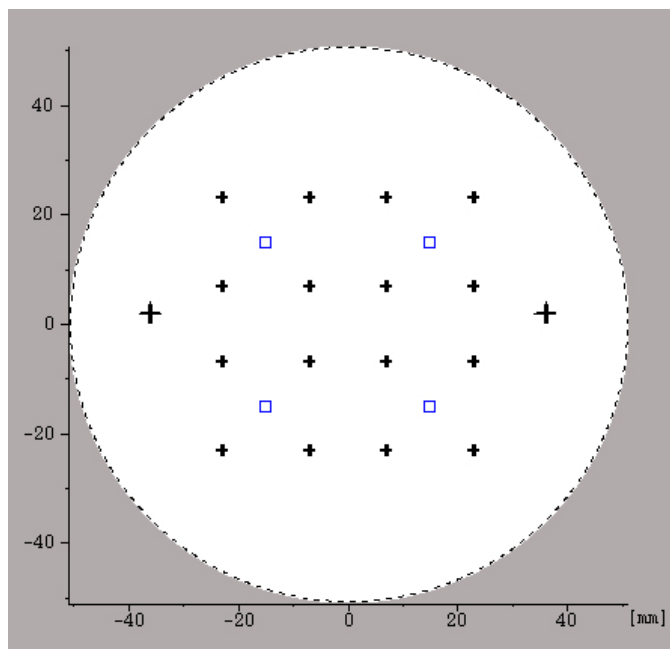


Figure A.1: Magnet-tipped chip example wafer layout, as rendered by the ACHK program in the JEOL software, for the chip design and release (etch slits) layer. The P -mark and Q -mark for this layer are the large crosses shown near the left and right edges of the wafer, respectively; the P -mark is located at (x,y) coordinates $(-36 \text{ mm}, 1 \text{ mm})$ and the Q -mark is located at $(+36 \text{ mm}, 1 \text{ mm})$. The four blue squares designate the four magnet-tipped chip dies, which are centered at $(\pm 15 \text{ mm}, \pm 15 \text{ mm})$. The small crosses designate the chip marks. For this layer, the local marks are 8 mm in each x and y from the center of each magnet-tipped chip die.

of the wafer is $(0,0)$ and the positive directions move to the right and downward, whereas the SETWFR (for global marks) and CHIPAL (for local marks) locations are listed in the material coordinate system, in which the center of the wafer is $(0,0)$ and the positive directions are to the right and upward. Note also that on the JEOL 9300 system, the 4" chuck has two slots, "A" (stage-coordinate center is $x = 190,000 \mu\text{m}$ and $y = 65,000 \mu\text{m}$) and "B" (stage-coordinate center is $x = 100,000 \mu\text{m}$ and $y = 175,000 \mu\text{m}$), whereas the JEOL 6300 system has two identical single-slot 4" chucks, each with their stage-coordinate center at $x = 105,000 \mu\text{m}$ and $y = 85,000 \mu\text{m}$. In Table A.1, the AGCRG positions are calculated by $x = (x \text{ center position}) + (P\text{-point value})$ and $y = (y \text{ center position}) - (Q\text{-point value})$.

A.2 Alignment Marks

1. Resist bilayer

In the e-beam lithography hood:

- (a) 8% 495,000 MW PMMA in anisole, spin 70 seconds at 3000 rpm, bake at 170°C for 20 minutes
- (b) 2% 950,000 MW PMMA in methyl isobutyl ketone (MIBK), spin 60 seconds at 4000 rpm, bake at 170°C for 15 minutes

2. E-beam lithography patterning

- (a) Use the appropriate alignment mark file in the JEOL; Longenecker's file was called "jl_marks.sdf". The global and local marks were stored permanently in the JEOL pattern files.
- (b) Run the basic calibration sequence, including CURRNT, INITBE (3×), INITAE (3×), SFOCUS, PDEFBE, SUBDEFBE, and DISTBE. Running HEIMAP is not necessary if virtual marks are used.
- (c) Expose the wafer at an electron dose of 1800 $\mu\text{C cm}^{-2}$.

3. Developing the wafer

Soak the exposed wafer in premixed 1:3 (v/v) MIBK:IPA for 75 seconds. Spray with IPA and dry with the nitrogen gun.

4. Descuming the wafer

In the Glen 1000 Resist Strip system, center the wafer on shelf B. Use Program 3, 100 W for 60 seconds.

5. Electron gun evaporation: Ti/Pt (5/100 nm)

- (a) Check the life of the quartz crystal and replace if the conditions specified in the instrument's manual are exceeded. Load titanium (adhesion layer) and platinum (contrast material for e-beam lithography marks) targets.
- (b) For titanium: Ramp the power to 5% and wait a few minutes for the crucible to warm up. Continue to ramp at approximately 1% per minute until the rate is 2 Å/s (approximately 10% power). Open the shutter and deposit the 50 Å adhesion layer. Close the shutter and ramp the power back down at approximately 1% per minute.
- (c) For platinum: Ramp the power to 5% and wait for the system to warm up the new target. Continue to ramp at approximately 1% per minute until a rate of 2 to 2.5 Å/s is reached (anywhere from 15% to 25% power, depending on the amount of dephasing of the electron beam). Continuously check the lateral and longitudinal sweep, especially as the power exceeds 15%. Open the shutter and deposit 100 nm of platinum. Close the shutter and ramp the power down at 5% per minute.
- (d) Allow the chamber to cool for 10 minutes before venting the system and removing the wafer.

6. Resist liftoff

- (a) Mix a 1:1 (v/v) solution of methylene chloride and acetone.
- (b) Sonicate the wafer in the methylene chloride and acetone solution for at least 10 minutes, and for at least 1 minute after all platinum has detached from the wafer surface.
- (c) Rinse the wafer with IPA as you remove the wafer from the solution, making sure that all excess metal specks are removed.
- (d) Quickly dry the wafer with the nitrogen gun.

- (e) Pour waste in the appropriate waste bottle. Rinse the container 3× with IPA (pour into waste container) before rinsing 3× with water (pour down drain).

A.3 Chip Design and Release

1. Resist layer

8% 495,000 MW PMMA in anisole, spin 75 seconds at 2000 rpm, bake at 170°C for 20 minutes.

Note that if 8% 495,000 MW PMMA in anisole is not available, a suitable replacement is:

11% 495,000 MW PMMA in anisole, spin 70 seconds at 4000 rpm, bake at 170°C for 20 minutes.

2. E-beam lithography patterning

- (a) Use the appropriate alignment mark file in the JEOL; Longenecker's file was called "etchslits_201106.sdf".
- (b) Run the basic calibration sequence, including CURRNT, INITBE (3×), INITAE (3×), SFOCUS, PDEFBE, SUBDEFBE, and DISTBE. Running HEIMAP is not necessary if virtual marks are used.
- (c) Run AGCRG, SETWFR, and CHIPAL using the appropriate values in Table A.1. For SETWFR, all sweep positions and sweep widths were set to 100 μm. For CHIPAL, the sweep position was set to 15 μm and the sweep width was set to 10 μm.
- (d) If the global marks cannot be found automatically using AGCRG, locate the marks manually and enter the offset between the expected position and actual position in the "material center offset" positions in SETWFR (using the offset

calculation guide in Table A.1). Also enter the offset values in the appropriate jdf file. Offsets do not affect the CHIPAL calibration. On the JEOL 6300, offsets of up to 1 mm were observed and manual alignment was routinely needed. On the JEOL 9300, offsets were minimal and the global marks were almost always found automatically.

(e) Expose the wafer at an electron dose of $1600 \mu\text{C cm}^{-2}$.

3. Developing the wafer

Soak the exposed wafer in premixed 1:3 (v/v) MIBK:IPA for 75 seconds. Spray with IPA and dry with the nitrogen gun.

4. Descuming the wafer

In the Glen 1000 Resist Strip system, center the wafer on shelf B. Use Program 3, 100 W for 60 seconds.

5. Etching the etch slits to define the chip bodies

(a) Use the Oxford PlasmaLab 80+ RIE System # 2 (commonly called the Oxford 82).

(b) Clean the chamber for 10 minutes using the standard oxygen clean recipe (50 sccm O_2 , 150 W, 60 mTorr).

(c) Stop the automatic vent cycle, evacuate the chamber to base pressure, and season the chamber for five minutes using the sulfur hexafluoride and oxygen ($\text{SF}_6:\text{O}_2$) recipe (30 sccm SF_6 , 10 sccm O_2 , 200 W, 200 mTorr).

(d) Vent the chamber and load the wafer. Center the wafer on the substrate electrode and fix it in place using clean quartz pieces.

(e) Etch the device layer silicon on the wafer for 40 seconds using the same $\text{SF}_6:\text{O}_2$ recipe as Step 5(c).

6. Visual inspection of etch completion

After the slits have been etched, the underlying green BOX SiO₂ layer is visible. The complete removal of the silicon can be confirmed using an optical microscope by checking for a color change from gray to green in these exposed regions.

7. Resist liftoff

- (a) Mix a 1:1 (v/v) solution of methylene chloride and acetone.
- (b) Sonicate the wafer in the methylene chloride and acetone solution for 10 minutes.
- (c) Rinse the wafer with IPA as it is removed from the solution and quickly dry the wafer with the nitrogen gun.

8. Suspension of the chips by BOE etching

- (a) Fill one plastic tub 1/3 full with 6:1 buffered oxide etch (BOE). Fill two additional plastic tubs 3/4 full with deionized water.
- (b) Soak the wafer in BOE for 50 minutes.¹
- (c) Quickly transfer the wafer to the first water bath and soak for 30 minutes to flush the BOE from the suspended region under the chips.
- (d) Transfer the wafer to the second water bath and carry the tub to an IPA-compatible spinner.
- (e) Transfer the wafer to an IPA bath.
- (f) Spin-dry the wafer for 75 seconds at 2000 rpm. Spin drying successfully dries the wafer while preventing stiction of the chips.

9. Visual inspection of suspension

Release chips (Section 3.7.3) were added to the dies so that it would be easy to confirm

¹The etch has been calibrated for a BOE bath without a stir bar; adding a stir bar may decrease the required etch time.

completion of the suspension etch. If the chips are fully suspended, the similarly-designed release chips become free-standing and are absent or moved on the silicon surface. Optical microscopy can be used to assess the status of the release chips.

A.4 Nickel or Cobalt Nanomagnet Deposition

1. Resist bilayer

For nanomagnets up to 200 nm thick:

- (a) 8% 495,000 MW PMMA in anisole, spin 70 seconds at 3000 rpm, bake at 170°C for 20 minutes
- (b) 2% 950,000 MW PMMA in MIBK, spin 60 seconds at 4000 rpm, bake at 170°C for 15 minutes

2. E-beam lithography patterning

- (a) Use the appropriate alignment mark file in the JEOL; Longenecker's file was called "mags_201106.sdf". The guide boxes — which were centered on the dies, were 2 mm in length, and had line widths of 2 μm — were used to more easily locate and focus the magnet-tipped chips during SEM analysis.
- (b) Run the basic calibration sequence, including CURRNT, INITBE (3 \times), INITAE (3 \times), SFOCUS, PDEFBE, SUBDEFBE, and DISTBE. Running HEIMAP is not necessary if virtual marks are used.
- (c) Run AGCRG, SETWFR, and CHIPAL using the appropriate values in Table [A.1](#). For SETWFR, all sweep positions and sweep widths were set to 100 μm . For CHIPAL, the sweep position was set to 15 μm and the sweep width was set to 10 μm .

- (d) If the global marks cannot be found automatically using AGCRG, locate the marks manually and enter the offset between the expected position and actual position in the “material center offset” positions in SETWFR (using the offset calculation guide in Table A.1). Also enter the offset values in the appropriate jdf file.
- (e) Expose the wafer at an electron dose of $1600 \mu\text{C cm}^{-2}$.

3. Developing the wafer

- (a) Soak the exposed wafer in premixed 1:3 (v/v) MIBK:IPA for 75 seconds.
- (b) Use a squirt bottle to gently spray the wafer with IPA. Avoid spraying liquid directly over the suspended chips; instead spray only in the center and along the edges of the wafer.
- (c) Spin-dry the wafer for 75 seconds at 2000 rpm. Since the wafer now has suspended chips, it must be handled delicately and drying the wafer with the nitrogen gun is not recommended. This alternate spin-drying procedure is used to gently dry the wafer.

4. Descuming the wafer

In the Glen 1000 Resist Strip system, center the wafer on shelf B. Use Program 3, 100 W for 60 seconds.

5. Electron gun evaporation: Ti/Ni/Pt (5/100/10 nm) or Ti/Co/Pt (5/100/10 nm)

- (a) Check the life of the quartz crystal and replace if the conditions specified in the instrument’s manual are exceeded. Loading a witness sample is recommended; witness samples can be used to confirm the total film thickness after deposition. The witness samples used in this work, which were freely available in the CNF, were small silicon chips with ~ 1 mm wide lines (with a pitch of ~ 2 mm) that were

patterned in photolithography resist. Load titanium (adhesion layer), platinum (capping layer), and nickel or cobalt (magnetic layer) targets. It is recommended that crucibles containing magnetic material be stored separately from common-access crucibles to prevent any chance of contamination.

- (b) For titanium: Ramp the power to 5% and wait a few minutes for the crucible to warm up. Continue to ramp at approximately 1% per minute until the rate is 2 Å/s (approximately 10% power). Open the shutter and deposit the 50 Å adhesion layer. Close the shutter and ramp the power back down at approximately 1% per minute.
- (c) For nickel: Ramp the power to 5% and wait for the system to warm up the new crucible. Continue to ramp 0.5% per minute until a rate of 2.5 Å/s (approximately 12% power). Prevent spitting of the material by reducing the power 0.5% and soaking the material for at least 3 minutes if spitting is observed. Consistently monitor the lateral and longitudinal sweep, especially since nickel deflects the beam differently as it becomes molten. Open the shutter and deposit 100 nm of material. Close the shutter and ramp the power down at 1% per minute.
- (d) For cobalt: Ramp the power to 5% and wait for the system to warm up the new crucible. Continue to ramp 0.5% per minute until a rate of 2.5 Å/s (approximately 11% power). Prevent spitting of the material by reducing the power 0.5% and soaking the material for at least 3 minutes if spitting is observed. Consistently monitor the lateral and longitudinal sweep, especially since cobalt deflects the beam differently as it becomes molten. Open the shutter and deposit 100 nm of material. Close the shutter and ramp the power down at 1% per minute.
- (e) For platinum: Ramp the power to 5% and wait for the system to warm up the new target. Continue to ramp at approximately 1% per minute until a rate of 2 to 2.5 Å/s is reached (anywhere from 15% to 25% power, depending on the

amount of dephasing of the electron beam). Continuously check the lateral and longitudinal sweep, especially as the power exceeds 15%. Open the shutter and deposit 10 nm of platinum. Close the shutter and ramp the power down at 5% per minute.

- (f) Allow the chamber to cool for at least 10 minutes and until the chamber temperature is at or below room temperature of 68°F prior to venting and removing the wafer.

6. Resist liftoff

- (a) Mix a 1:1 (v/v) solution of methylene chloride and acetone.
- (b) Sonicate the wafer in the methylene chloride and acetone solution for at least 10 minutes, and for at least 1 minute after all material has been stripped off of the wafer surface. Sonication has been shown to minimize rough edges around the nanomagnets that are likely due to magnetic material propagating up the resist side walls during deposition.
- (c) Rinse the wafer using a squirt bottle containing IPA as the wafer is removed from the solution, making sure that all excess metal specks are removed. Avoid spraying liquid directly over the suspended chips; instead spray only in the center and along the edges of the wafer.
- (d) Spin-dry the wafer for 75 seconds at 2000 rpm.

A.5 Silicon Underetch of U-Shaped Etch Pits

1. Resist layer

8% 495,000 MW PMMA in anisole, spin 75 seconds at 2000 rpm, bake at 115°C for 40

minutes.

Note that if 8% 495,000 MW PMMA in anisole is not available, a suitable replacement is:

11% 495,000 MW PMMA in anisole, spin 70 seconds at 4000 rpm, bake at 115°C for 40 minutes.

2. E-beam lithography patterning

- (a) Use the appropriate alignment mark file in the JEOL; Longenecker's file was called "pits_201106.sdf".
- (b) Run the basic calibration sequence, including CURRNT, INITBE (3×), INITAE (3×), SFOCUS, PDEFBE, SUBDEFBE, and DISTBE. Running HEIMAP is not necessary if virtual marks are used.
- (c) Run AGCRG, SETWFR, and CHIPAL using the appropriate values in Table A.1. For SETWFR, all sweep positions and sweep widths were set to 100 μm. For CHIPAL, the sweep position was set to 15 μm and the sweep width was set to 10 μm.
- (d) If the global marks cannot be found automatically using AGCRG, locate the marks manually and enter the offset between the expected position and actual position in the "material center offset" positions in SETWFR (using the offset calculation guide in Table A.1). Also enter the offset values in the appropriate jdf file.
- (e) Expose the wafer at an electron dose of 1600 μC cm⁻².

3. Developing the wafer

- (a) Soak the exposed wafer in premixed 1:3 (v/v) MIBK:IPA for 75 seconds.
- (b) Use a squirt bottle to gently spray the wafer with IPA. Avoid spraying liquid

directly over the suspended chips; instead spray only in the center and along the edges of the wafer.

(c) Spin-dry the wafer for 75 seconds at 2000 rpm.

4. Descuming the wafer

In the Glen 1000 Resist Strip system, center the wafer on shelf B. Use Program 3, 100 W for 60 seconds.

5. Etching the etch slits to define the chip bodies

(a) Use the Oxford PlasmaLab 80+ RIE System # 2 (commonly called the Oxford 82).

(b) Clean the chamber for 10 minutes using the standard oxygen clean recipe (50 sccm O₂, 150 W, 60 mTorr).

(c) Stop the automatic vent cycle, evacuate the chamber again, and season the chamber for five minutes using the sulfur hexafluoride and oxygen (SF₆:O₂) recipe (30 sccm SF₆, 10 sccm O₂, 200 W, 200 mTorr).

(d) Vent the chamber and load the wafer. Center the wafer on the substrate electrode and fix in place using clean quartz pieces.

(e) Etch the device layer silicon on the wafer for 40 seconds using the same SF₆:O₂ recipe as Step 5(c). The etch time has been calibrated to create a 300 nm overhang of the nanomagnets.

6. Visual inspection of etch completion

During the U-shaped pit etching, pits are also dug into the top few micrometers of the handle silicon layer. Visual inspection with an optical microscope can provide tentative confirmation that the etch has been completed, but thorough characterization of the overhang can only be achieved by SEM analysis.

7. Resist liftoff

- (a) Mix a 1:1 (v/v) solution of methylene chloride and acetone.
- (b) Sonicate the wafer in the methylene chloride and acetone solution for 10 minutes.
- (c) Rinse the wafer with a squirt bottle containing IPA as the wafer is removed from the solution. Avoid spraying liquid directly over the suspended chips; instead spray only in the center and along the edges of the wafer.
- (d) Spin-dry the wafer for 75 seconds at 2000 rpm.

APPENDIX B

FOCUSED ION BEAM PROCESS FOR LIFT-OUT OF MAGNET-TIPPED CHIPS AND ATTACHMENT TO CANTILEVERS

In this Appendix, details are provided for the protocol used to remove completed magnet-tipped chips from their substrate and attach them to separately-fabricated attonewton-sensitivity cantilevers. The development of the magnet-tipped chips is discussed in Chapter 3 and the fabrication protocol is detailed in Appendix A. A detailed description of an integrated magnet-on-cantilever fabrication protocol is provided in Appendix A of Ref. 91; to fabricate blank cantilevers, start with Section A.5.

The focused ion beam (FIB) lift-out and attachment process was conducted using an FEI Strata 400 STEM FIB DualBeam system with both an electron beam and a gallium-ion beam. Images of the original and revised FIB process flows discussed in Chapter 3 are shown in Figures 3.5 and 3.8, respectively; note that in both figures, the electron beam images were rotated by 180° so that all images were viewed with the magnet-tipped chips oriented in the same direction. The dual-beam FIB instrument used for this work is located in the Cornell Center for Materials Research transmission electron microscopy facility. The ion beam is oriented at a 52° angle with respect to the electron beam. The stage can be tilted between 0° and 52° degrees to allow one beam or the other to be aligned perpendicular to the sample surface. In the procedure described in this Appendix, all work (other than setting the eucentric height) is done with the stage at 0° , such that the sample is viewed top-down with the electron beam and side-on with the ion beam.

It should be noted that this set of directions is meant to be used in conjunction with the tool's manual. The following directions include all sample-specific details and are meant to

be as complete as possible, but they are not exhaustive.

B.1 Loading in Samples and Setting Up for the Magnet-Tipped Chip Release

1. Start the FIB software and unload the shuttle.
2. Load a magnet-tipped chip onto carbon tape on one FIB mounting holder and blank cantilevers onto a second carbon-tape-coated FIB mounting holder. It is helpful to load all cantilevers parallel to each other, and to load a sacrificial cantilever in the center for setup work. Mount the holders in the shuttle, insert the shuttle into the FIB loadlock, and load the shuttle onto the FIB stage.
3. Often the Omniprobe probe needle, which is used to lift out magnet-tipped chips and attach them to cantilevers, has been dulled by previous use and needs to be replaced. If the probe needle needs to be exchanged, the main FIB chamber must be vented. A detailed procedure can be obtained from the tool manager — changing the probe needle requires special training.
4. Once the samples are loaded and the chamber is pumped down, check that the electron beam is set to:
 - (a) a voltage of 5 kV, and
 - (b) a current of 1.6 nA.
5. Turn on the electron beam and locate the magnet-tipped chip die. Rotate the sample so that the side tabs are at the bottom of the screen in the scanning electron microscopy (SEM) image (for the second-generation and third-generation chips in Section [3.7.1](#), this means that the magnets/fingers on the chips are pointed towards the left).

6. Locate a chip that is a few chips away from the first region of interest (close enough to be accurate for the desired chip, but far enough away to not damage the critical nanomagnet). Raise the stage to a working distance of 5 mm, adjust the focus and stigmation, and “link the z axis” over the device silicon.
7. Set the eucentric height by confirming that the edge of a feature remains in the same position for tilts $T = 0^\circ$ and $T = 52^\circ$.
8. Check that the ion beam is set to:
 - (a) a voltage of 30 kV,
 - (b) and a current of 28 pA.

Note that it is critical to not turn the beam on until the voltage and current have been confirmed; if the values are too high, the region of interest could be completely milled away in under a second. Also, when practicing to focus, stigmatize, and find the eucentric height with the ion beam, the ion beam current can be set lower to 9.7 pA; the rate of carbon contamination is slower when using a lower current. However, once the current is set to 28 pA for platinum deposition and milling, it should not be changed since changing the aperture shakes the system and could damage overconstrained systems when the needle is in contact with a sample.

9. Adjust the scan rotation of the ion beam to 180° (the side tab should now be at the top of the ion beam screen and at the bottom of the SEM screen).
10. Once the settings are confirmed, increase magnification (while the beam is still inactive). Note that the magnet-tipped chip being viewed during this step should still be one that is near a chip of interest but should itself not be used. Briefly turn on the beam, decreasing the magnification just enough to confirm that the same region of the chip can be viewed simultaneously by both the electron and ion beams. Quickly adjust the focus and stigmation of the ion beam. Turn the ion beam off.

11. Move to the magnet-tipped chip of interest and repeat Steps 6-8. From here on out, it is essential that the nanomagnet not be viewed by the ion beam to prevent gallium implantation into the magnet.

B.2 Releasing the Magnet-Tipped Chip from the Substrate

1. Confirm that the tilt is set to 0° . Insert the probe needle. Heat and insert the platinum deposition gun. Note that FIB-assisted chemical vapor deposition is used to convert the platinum precursor methylcyclopentadienyl(trimethyl)platinum(IV) into (carbon-containing) platinum metal.
2. Using the SEM mode, center the probe needle laterally over the side tab on the magnet-tipped chip. Lower the needle vertically until it is within a few micrometers of the tab. The steps of raising/lowering the probe needle when in close proximity to the nanomagnet are the most challenging of the entire lift-out and attachment process because the nanomagnet cannot be imaged while moving the probe needle. It is recommended that multiple test trials be conducted to determine the best method for each new user. It is also recommended that one trial test over an unimportant portion of the substrate be conducted each day and that the user watch the z -coordinate stage positions at the start and end of bringing the probe needle into position. These positions should be consistent throughout the day. It is critical to not overshoot how far the needle should be lowered; the needle will immediately bend or break, and excessive driving of the needle into the substrate could cause further damage to the sample and/or tool. Once the mock trials have been conducted, one method for successfully bringing the needle into position without imaging the magnet is to image the chip next to the chip of interest (in the direction opposite than the nanomagnet-tipped end of the chip) at high enough magnification to not view any other chips. Lower the probe needle in the z

direction while leaving the ion beam image on. As soon as the top of the needle comes into view, move the stage to the correct chip (and increase the magnification so that the nanomagnet is never viewed), and finish lowering the chip into position.

One additional word of caution with lowering the probe needle is that the x - y lateral motion of the probe needle is coupled to the z motion. As the probe needle is moved towards the top of the SEM screen, the probe moves downward in z ; when the probe needle is moved towards the bottom of the screen in the SEM pane, the probe needle moves up in z . Consistently check both screens to monitor the three-dimensional position of the probe needle.

3. Reduce the speed of the probe needle motion and gently bring the probe needle into contact with the side tab of the magnet-tipped chip. Deposit a rectangular patch of platinum to adhere the probe needle to the magnet-tipped chip. When depositing platinum, the rectangular box should have an area corresponding to $6 \text{ pA}/\mu\text{m}^2$; since the current is set to 28 pA , the total area should be approximately $4.5 \mu\text{m}$. The thickness of the platinum should be approximately $1 \mu\text{m}$.
4. To release the suspended chip from the substrate, mill away the back and side support tethers. The back tether should be milled at an angle, as shown in Figure 3.8. Note that in this figure, the electron beam images have been rotated by 180° for easier viewing.
5. Slowly lift the chip vertically away from the substrate at least $10 \mu\text{m}$.
6. To refine the chip shape to promote increased surface area for platinum adhesion once the chip is attached to a cantilever, mill two rectangles into the bottom side of the chip (opposite the side tab) and taper the thickness of the back edge of the chip by approximately 50%, as shown in Figure 3.8(b).
7. The probe needle and platinum deposition gun must be retracted before moving over to the cantilever. First the probe needle must be raised to the starting height (the z

height should be at the top of the ion-beam screen when at the lowest magnification) and then to the load/unload horizontal position (the x - y position should be near the bottom-left corner of the SEM screen when at a magnification of $100\times$). Once the probe needle has been moved to the proper load/unload position, first retract the probe needle and second retract the platinum deposition gun.

B.3 Adhering the Magnet-Tipped Chip to a Blank Cantilever and Removing the Probe Needle

1. Using the SEM mode, move to the location of the cantilevers and find the desired cantilever on which to mount the magnet-tipped chip. Rotate the stage so that the cantilever is pointing in the same direction as the magnet/finger on the magnet-tipped chip (for the second- and third-generation tips, this means the cantilever should point to the left). Focus and stigmatize on the leading edge of the tip and check the eucentric height. When using the ion beam, only image the portion of the cantilever in front of the paddle. Confirm that the cantilever is mostly straight (see Figure 4.2 for images of straight and bent cantilevers), since bent cantilevers are undesired for magnetic resonance force microscopy experiments.
2. Confirm that the tilt is set to $T = 0^\circ$. Insert the probe needle and the platinum deposition gun.
3. Move the probe needle (as done in Section B.2, Step 2) so that the magnet-tipped chip is centered laterally over the cantilever leading edge and hovering vertically a few micrometers above the cantilever surface. Note that it is now critical that the probe needle itself not be imaged by the ion beam any more than necessary while moving it down to the leading edge of the cantilever, since the magnet-tipped cantilever is

attached to the probe needle. In other words, the ion beam should be left off while lowering the needle except for a few low-magnification screen shots. Note also that since the cantilever is suspended 500 μm above the surrounding area, there is less of a chance of crashing the tip. The recommended procedure is to move the tip laterally (in SEM mode) to the region of the screen to the top of the cantilever. Then lower the probe (choose the same speed as for Section B.2, Step 2 and pay close attention to the time it takes to lower it to the appropriate height), capturing a few quick, low-magnification screen shots to confirm the position. As a higher comfort level is gained with this step, fewer screen shots will be needed; three or less screen shots were needed when conducting the work in Chapters 3-5.

4. Lower the speed of the probe needle movement. Confirm that the horizontal alignment is as-desired right before the chip and cantilever come into contact. Gently lower the magnet-tipped chip into contact with the cantilever. If the cantilever is bent slightly down from the chip at the leading edge (the chip and cantilever will always be in contact at the base of the chip), slowly pull up on the probe needle. Surface forces will keep the chip and cantilever “stuck” together for a small vertical window; retracting the probe needle slightly has been shown to improve chip and cantilever alignment.
5. Once the alignment is set, the chip and cantilever can be adhered together. Confirm that the magnet is out-of-range of the ion beam. Check the ion beam focus and stigmation. Define three platinum welding boxes: one angled box used to join the base of the chip with the back of the cantilever, and two additional boxes that are slightly larger than each of the rectangles that were FIB milled into the magnet-tipped chip body in Section B.2, Step 6. Deposit approximately 1 μm of platinum at each position. Note that the platinum adhesion points can be seen in the side-on image in Figure 3.8(c); again, the electron beam images in this figure were rotated by 180° for simplicity.

6. Once the chip is adhered to the cantilever, the chip-on-cantilever system is overconstrained, and the probe needle should be removed as quickly as possible. First define a small, angled silicon etch box to mill the narrow silicon support tether closest to the leading edge of the chip. The milling should only take a few seconds, so monitor it closely. Second, define a straight, relatively thin silicon etch box to mill the remaining portion of the side tab. Again, the milling should be quite quickly. As soon as the chip-on-cantilever is milled free from the side tab and probe needle, the cantilever will likely move downward (see the side-on image in Figure 3.8(d)). This is because the probe needle has been observed to drift upward with time.
7. At this point, the magnet-tipped chip has been mounted onto the cantilever. Slowly move the probe needle so that it is at least 20 μm above the cantilever. Move the ion beam image and/or stage so that the cantilever is well out of view of the beam at reduced magnification.
8. If the same probe needle will be used again for a subsequent sample, clean up the probe needle by increasing the ion beam current above 1 nA. Note that at this current the cantilever must be well out of view of the beam because it would be milled away in seconds even in imaging mode. Focus and stigmatize the beam at this new current, mill the chip and platinum adhesion point, and sharpen the tip.
9. Regardless of whether the probe needle will be replaced before being used again, the needle must be moved to the load/unload position before being retracted, as was done in Section B.2, Step 7. The probe needle should first be raised vertically to be at the top of the ion-beam screen when at the lowest magnification, and then the probe needle should be moved laterally to be near the bottom-left corner of the SEM screen when at a magnification of $100\times$. Once the probe needle has been moved to the proper load/unload position, first retract the probe needle and second retract the platinum deposition gun.

10. If additional samples will be lifted out, return to Section [B.1](#), Step 5. If all FIB work is complete, move on to Section [B.4](#).

B.4 Unloading the Completed Magnet-Tipped Cantilevers

1. Confirm that the probe needle and platinum deposition gun have been retracted. Turn off the platinum deposition gun heater.
2. Turn off the electron beam and ion beam.
3. Unload the shuttle into the loadlock.
4. Vent the loadlock and remove the shuttle.
5. The cantilevers are firmly adhered to the carbon tape on the mounting grid, so removal of the cantilever is a delicate process. Narrow tweezers with rounded ends are recommended. Gently take hold of the cantilever on the sides of the cantilever die. Rotate the cantilever and gently lift up, tilting to one side if necessary to loosen the tape on one side first. Maintain tension on the tweezers as the cantilever begins to release. Once the cantilever is released, it can be stored in a Gel-Pak.
6. It is recommended that the magnet-tipped chip die remain attached to the FIB mounting holder once it is attached; removal would likely break the chip. Store the mounting holder in a dust-proof container.
7. Return the empty shuttle to the loadlock and pump down the loadlock. Follow the remaining shut down procedures for the tool.

“And that’s all I have to say about that.”

- Forrest Gump

BIBLIOGRAPHY

- [1] <http://www.rcsb.org/>. 1
- [2] M. J. Rust, M. Bates, and X. Zhuang, Sub-diffraction-limit imaging by stochastic optical reconstruction microscopy (STORM), *Nat. Methods* **3**, 793 (2006). 1
- [3] E. Betzig et al., Imaging intracellular fluorescent proteins at nanometer resolution, *Science* **313**, 1642 (2006).
- [4] S. T. Hess, T. P. Girirajan, and M. D. Mason, Ultra-high resolution imaging by fluorescence photoactivation localization microscopy, *Biophys. J.* **91**, 4258 (2006). 1
- [5] S. A. Jones, S.-H. Shim, J. He, and X. Zhuang, Fast, three-dimensional super-resolution imaging of live cells, *Nat. Methods* **8**, 499 (2011). 1
- [6] Z. H. Zhou, Atomic resolution cryo electron microscopy of macromolecular complexes, *Adv. Protein Chem. Struct. Biol.* **82**, 1 (2011). 1
- [7] A. Bartesaghi and S. Subramaniam, Membrane protein structure determination using cryo-electron tomography and 3D image averaging, *Curr. Opin. Struct. Biol.* **19**, 402 (2009). 1
- [8] R. I. Koning and A. J. Koster, Cryo-electron tomography in biology and medicine, *Ann. Anat.* **191**, 427 (2009). 1
- [9] R. Fernandez-Busnadiego et al., Insights into the molecular organization of the neuron by cryo-electron tomography, *J. Electron Microscopy* **60**, S137 (2011). 1, 7
- [10] R. L. Felts et al., 3D visualization of HIV transfer at the virological synapse between dendritic cells and T cells, *Proc. Natl. Acad. Sci. U.S.A.* **107**, 13336 (2010). 1, 7
- [11] J. L. S. Milne and S. Subramaniam, Cryo-electron tomography of bacteria: Progress, challenges and future prospects, *Nat. Rev. Microbiol.* **7**, 666 (2009). 1, 7

- [12] C. L. Degen, M. Poggio, H. J. Mamin, C. T. Rettner, and D. Rugar, Nanoscale magnetic resonance imaging, *Proc. Natl. Acad. Sci. U.S.A.* **106**, 1313 (2009). [1](#), [1.1](#), [1.1](#), [1.1](#), [1.3](#), [2.1](#), [2.2](#), [2.6](#), [3.6](#), [4.4](#), [5.1](#), [5.2](#), [5.2.3](#), [5.2.4](#), [5.4](#), [5.6](#), [6.1](#), [6.5](#), [7](#)
- [13] J. A. Sidles, Noninductive detection of single-proton magnetic resonance, *Appl. Phys. Lett.* **58**, 2854 (1991). [1](#), [1.1](#)
- [14] D. Rugar, C. S. Yannoni, and J. A. Sidles, Mechanical detection of magnetic resonance, *Nature* **360**, 563 (1992). [1.1](#)
- [15] D. Rugar et al., Force detection of nuclear magnetic resonance, *Science* **264**, 1560 (1994). [1.1](#)
- [16] J. A. Sidles et al., Magnetic resonance force microscopy, *Rev. Mod. Phys.* **67**, 249 (1995). [1.1](#)
- [17] S. Kuehn, S. A. Hickman, and J. A. Marohn, Advances in mechanical detection of magnetic resonance, *J. Chem. Phys.* **128**, 052208 (2008). [1.2.2](#), [1.2.2](#), [5.2.1](#), [5.6](#)
- [18] M. Poggio and C. L. Degen, Force-detected nuclear magnetic resonance: Recent advances and future challenges, *Nanotechnology* **21**, 342001 (2010). [1](#), [1.1](#)
- [19] Z. H. Zhou, Towards atomic resolution structural determination by single-particle cryo-electron microscopy, *Curr. Opin. Struct. Biol.* **18**, 218 (2008). [1](#)
- [20] E. I. Tocheva, Z. Li, and G. J. Jensen, Electron cryotomography, *Cold Spring Harbor Perspect. Biol.* **2**, a003442 (2010).
- [21] E. V. Orlova and H. R. Saibil, Structural analysis of macromolecular assemblies by electron microscopy, *Chem. Rev.* **111**, 7710 (2011). [1](#)

- [22] L. Zhang and G. Ren, IPET and FETR: Experimental approach for studying molecular structure dynamics by cryo-electron tomography of a single-molecule structure, *PLoS ONE* **7**, e30249 (2012). [1](#)
- [23] S. Mathivanan, C. J. Fahner, G. E. Reid, and R. J. Simpson, Exocarta 2012: Database of exosomal proteins, RNA and lipids, *Nucl. Acids Res.* **40**, D1241 (2011). [1](#), [7](#)
- [24] S. Wu et al., Fabs enable single particle cryoEM studies of small proteins, *Structure* **20**, 582 (2012). [1](#), [7](#)
- [25] D. Rugar, R. Budakian, H. J. Mamin, and B. W. Chui, Single spin detection by magnetic resonance force microscopy, *Nature* **430**, 329 (2004). [1](#), [1.1](#), [1.3](#), [2.1](#), [2.2](#), [2.6](#), [5.1](#), [5.4](#)
- [26] P. P. Borbat, A. J. Costa-Filho, K. A. Earle, J. K. Moscicki, and J. H. Freed, Electron spin resonance in studies of membranes and proteins, *Science* **291**, 266 (2001). [1](#)
- [27] O. Schiemann et al., A PELDOR-based nanometer distance ruler for oligonucleotides, *J. Amer. Chem. Soc.* **126**, 5722 (2004).
- [28] P. P. Borbat, J. H. Davis, S. E. Butcher, and J. H. Freed, Measurement of large distances in biomolecules using double-quantum filtered refocused electron spin-echoes, *J. Am. Chem. Soc.* **126**, 7746 (2004).
- [29] S. Y. Park et al., Reconstruction of the chemotaxis receptor-kinase assembly, *Nat. Struct. Mol. Biol.* **13**, 400 (2006). [1](#)
- [30] E. W. Moore et al., Scanned-probe detection of electron spin resonance from a nitroxide spin probe, *Proc. Natl. Acad. Sci. U.S.A.* **106**, 22251 (2009). [1](#), [1.1](#), [1.1](#), [2.1](#), [2.2](#), [5.1](#), [6.1](#), [6.4.3](#), [6.4.3](#), [6.4.5](#), [7](#)

- [31] Q. Cai et al., Site-directed spin labeling measurements of nanometer distances in nucleic acids using a sequence-independent nitroxide probe, *Nucl. Acids Res.* **34**, 4722 (2006). [1](#)
- [32] P. Z. Qin, K. Hideg, J. Feigon, and W. L. Hubbell, Monitoring RNA base structure and dynamics using site-directed spin labeling, *Biochemistry* **42**, 67726783 (2003).
- [33] Q. Cai et al., Nanometer distance measurements in RNA using site-directed spin labeling, *Biophys. J.* **93**, 2110 (2007). [1](#)
- [34] J. H. Zhang, G. Xiao, R. P. Gunsalus, and W. L. Hubbell, Phosphorylation triggers domain separation in the DNA binding response regulator NarL, *Biochemistry* **42**, 2552 (2003). [1](#)
- [35] C. J. Brabec, M. Heeney, I. McCulloch, and J. Nelson, Influence of blend microstructure on bulk heterojunction organic photovoltaic performance, *Chem. Soc. Reviews* **40**, 1185 (2011). [1](#)
- [36] R. Giridharagopal and D. S. Ginger, Characterizing morphology in bulk heterojunction organic photovoltaic systems, *J. Phys. Chem. Lett.* **1**, 1160 (2010). [1](#)
- [37] M. Chiesa et al., Correlation between surface photovoltage and blend morphology in polyfluorene-based photodiodes, *Nano Lett.* **5**, 559 (2005).
- [38] D. C. Coffey and D. S. Ginger, Time-resolved electrostatic force microscopy of polymer solar cells, *Nat. Mater.* **5**, 735 (2006).
- [39] V. Palermo et al., The relationship between nanoscale architecture and function in photovoltaic multichromophoric arrays as visualized by Kelvin probe force microscopy, *J. Am. Chem. Soc.* **130**, 14605 (2008).

- [40] E. J. Spadafora, R. Demadrille, B. Ratier, and B. Grevin, Imaging the carrier photogeneration in nanoscale phase segregated organic heterojunctions by Kelvin probe force microscopy, *Nano Lett.* **10**, 3337 (2010).
- [41] J. L. Luria et al., Spectroscopic imaging of photopotentials and photoinduced potential fluctuations in a bulk heterojunction solar cell film, *ACS Nano* **6**, 9392 (2012). [1](#)
- [42] S. S. van Bavel and J. Loos, Volume organization of polymer and hybrid solar cells as revealed by electron tomography, *Adv. Funct. Mater.* **20**, 3217 (2010). [1](#)
- [43] B. Xue et al., Vertical stratification and interfacial structure in P3HT:PCBM organic solar cells, *J. Phys. Chem. C* **114**, 15797 (2010). [1](#)
- [44] N. Bloembergen, Theory of the variation of the nuclear quadrupole interaction in covalent bonds with applied electric field, *J. Chem. Phys.* **35**, 1131 (1961). [1](#)
- [45] R. W. Dixon and N. Bloembergen, Electrically induced perturbations of halogen nuclear quadrupole interactions in polycrystalline compounds. I. Phenomenological theory and experimental results, *J. Chem. Phys.* **41**, 1720 (1964). [7](#)
- [46] T. Kushida and K. Saiki, Shift of nuclear quadrupole resonance frequency by electric fields, *Phys. Rev. Lett.* **7**, 9 (1961).
- [47] J. G. Kempf and D. P. Weitekamp, Method for atomic-layer-resolved measurement of polarization fields by nuclear magnetic resonance, *J. Vac. Sci. Technol. B* **18**, 2255 (2000). [1](#), [7](#)
- [48] H. J. Mamin, C. T. Rettner, M. H. Sherwood, L. Gao, and D. Rugar, High field-gradient dysprosium tips for magnetic resonance force microscopy, *Appl. Phys. Lett.* **100**, 013102 (2012). [1](#), [1.1](#), [1.2.2](#), [2.1](#), [2.6](#), [3.6](#), [5.1](#), [5.4](#), [c](#), [d](#)

- [49] R. A. Grassucci, D. J. Taylor, and J. Frank, Preparation of macromolecular complexes for cryo-electron microscopy, *Nat. Protoc.* **2**, 3239 (2007). [1](#), [7](#)
- [50] M. Marko, C. Hsieh, R. Schalek, J. Frank, and C. Mannella, Focused-ion-beam thinning of frozen-hydrated biological specimens for cryo-electron microscopy, *Nat. Meth.* **4**, 215 (2007). [1](#), [7](#)
- [51] K. Wago, D. Botkin, C. S. Yannoni, and D. Rugar, Paramagnetic and ferromagnetic resonance imaging with a tip-on-cantilever magnetic resonance force microscope, *Appl. Phys. Lett.* **72**, 2757 (1998). [1](#), [1.1](#), [5.1](#)
- [52] B. C. Stipe et al., Electron spin relaxation near a micron-size ferromagnet, *Phys. Rev. Lett.* **87**, 277602 (2001). [1.1](#), [1.1](#), [5.6](#)
- [53] H. J. Mamin, R. Budakian, B. W. Chui, and D. Rugar, Detection and manipulation of statistical polarization in small spin ensembles, *Phys. Rev. Lett.* **91**, 207604 (2003). [1](#), [1.1](#), [1.3](#), [2.1](#), [2.2](#), [2.6](#), [5.1](#), [5.4](#), [6.4.3](#), [7](#)
- [54] K. C. Fong, M. R. Herman, P. Banerjee, D. V. Pelekhov, and P. C. Hammel, Spin lifetime in small ensembles of electron spins measured by magnetic resonance force microscopy, *Phys. Rev. B* **84**, 220405 (2011). [1](#), [1.3](#), [5.1](#), [5.4](#)
- [55] S. R. Garner, S. Kuehn, J. M. Dawlaty, N. E. Jenkins, and J. A. Marohn, Force-gradient detected nuclear magnetic resonance, *Appl. Phys. Lett.* **84**, 5091 (2004). [1.1](#), [1.1](#), [1.1](#), [2.1](#), [6.4.3](#)
- [56] H. J. Mamin, R. Budakian, B. W. Chui, and D. Rugar, Magnetic resonance force microscopy of nuclear spins: Detection and manipulation of statistical polarization, *Phys. Rev. B* **72**, 024413 (2005). [1](#), [1.1](#), [1.1](#), [1.3](#), [2.1](#), [5.1](#), [5.4](#), [6.4.3](#)

- [57] K. J. Bruland, W. M. Dougherty, J. L. Garbini, J. A. Sidles, and S. H. Chao, Force-detected magnetic resonance in a field gradient of 250000 Tesla per meter, *Appl. Phys. Lett.* **73**, 3159 (1998). [1](#), [1.1](#), [1.3](#), [5.1](#), [5.4](#)
- [58] J. G. Longenecker et al., High-gradient nanomagnets on cantilevers for sensitive detection of nuclear magnetic resonance, *ACS Nano* **6**, 9637 (2012). [1.1](#), [1.1](#), [1.2.1](#), [1.2.1](#), [1.3](#), [3.6](#), [3.9](#), [5.4](#), [5.4](#), [6.4.3](#), [6.4.3](#)
- [59] H. J. Mamin, M. Poggio, C. L. Degen, and D. Rugar, Nuclear magnetic resonance imaging with 90-nm resolution, *Nat. Nanotechnol.* **2**, 301 (2007). [1.1](#), [1.1](#)
- [60] M. Poggio, C. L. Degen, C. T. Rettner, H. J. Mamin, and D. Rugar, Nuclear magnetic resonance force microscopy with a microwire RF source, *Appl. Phys. Lett.* **90**, 263111 (2007). [1.1](#), [4.4](#), [5.1](#), [5.2](#), [5.2.3](#), [6.1](#), [6.5](#)
- [61] L. Chen, J. G. Longenecker, E. W. Moore, and J. A. Marohn, Long-lived frequency shifts observed in a magnetic resonance force microscope experiment following microwave irradiation of a nitroxide spin probe, in preparation (2012). [1.1](#), [6.1](#), [6.4.5](#)
- [62] O. Züger and D. Rugar, Magnetic resonance detection and imaging using force microscope techniques, *J. Appl. Phys.* **75**, 6211 (1994). [1.1](#), [1.1](#)
- [63] K. Wago, O. Züger, R. Kendrick, C. S. Yannoni, and D. Rugar, Low-temperature magnetic resonance force detection, *J. Vac. Sci. Technol. B* **14**, 1197 (1996).
- [64] Z. Zhang, M. L. Roukes, and P. C. Hammel, Sensitivity and spatial resolution for electron-spin-resonance detection by magnetic resonance force microscopy, *J. Appl. Phys.* **80**, 6931 (1996).
- [65] K. Wago et al., Magnetic resonance force detection and spectroscopy of electron spins in phosphorus-doped silicon, *Rev. Sci. Instrum.* **68**, 1823 (1997). [1.1](#)

- [66] T. D. Stowe et al., Attonewton force detection using ultrathin silicon cantilevers, *Appl. Phys. Lett.* **71**, 288 (1997). [1.1](#), [1.2.1](#), [2.1](#), [2.2](#), [3.3](#)
- [67] H. Mamin and D. Rugar, Sub-attonewton force detection at millikelvin temperatures, *Appl. Phys. Lett.* **79**, 3358 (2001). [5.2.1](#)
- [68] N. E. Jenkins et al., Batch fabrication and characterization of ultrasensitive cantilevers with submicron magnetic tips, *J. Vac. Sci. Technol. B* **22**, 909 (2004). [1.1](#), [1.2.1](#), [2.1](#), [2.2](#), [3.3](#), [3.5](#), [4.3.2](#)
- [69] R. Budakian, H. Mamin, B. Chui, and D. Rugar, Creating order from random fluctuations in small spin ensembles, *Science* **307**, 408 (2005). [1.1](#), [2.1](#)
- [70] C. L. Degen, M. Poggio, H. J. Mamin, and D. Rugar, Role of spin noise in the detection of nanoscale ensembles of nuclear spins, *Phys. Rev. Lett.* **99**, 250601 (2007). [1.2](#), [2.1](#), [2.6](#), [5.2.4](#)
- [71] F. Xue, D. Weber, P. Peddibhotla, and M. Poggio, Measurement of statistical nuclear spin polarization in a nanoscale GaAs samples, *Phys. Rev. B* **84**, 205328 (2011). [1.1](#), [2.1](#), [2.6](#)
- [72] C. P. Slichter, *Principles of Magnetic Resonance, 3rd Ed.*, Springer, New York, 1990. [1.1](#)
- [73] O. Züger, S. T. Hoen, C. S. Yannoni, and D. Rugar, Three-dimensional imaging with a nuclear magnetic resonance force microscope, *J. Appl. Phys.* **79**, 1881 (1996). [1.1](#)
- [74] S. H. Chao, W. M. Dougherty, J. L. Garbini, and J. A. Sidles, Nanometer-scale magnetic resonance imaging, *Rev. Sci. Instrum.* **75**, 1175 (2004).
- [75] S. Tsuji, Y. Yoshinari, H. Park, and D. Shindo, Three dimensional magnetic resonance

- imaging by magnetic resonance force microscopy with a sharp magnetic needle, *J. Magn. Res.* **178**, 325 (2006). [1.1](#)
- [76] J. G. Kempf and J. A. Marohn, Nanoscale Fourier-transform imaging with magnetic resonance force microscopy, *Phys. Rev. Lett.* **90**, 087601 (2003). [1.1](#), [6.1](#)
- [77] R. Budakian, NanoMRI using nanowire mechanical resonators, NanoMRI Conference 2012; Ascona, Switzerland, July 22 - 27, 2012. [1.1](#)
- [78] N. E. Jenkins, *Expanding the Limits of Magnetic Resonance Force Microscopy*, PhD thesis, Cornell University, 2007. [1.2](#)
- [79] S. Kuehn, *Force-Gradient Detected Nuclear Magnetic Resonance and the Origins of Noncontact Friction*, PhD thesis, Cornell University, 2007. [1.2](#), [6.1](#)
- [80] Y. Wang, J. Henry, A. Zehnder, and M. Hines, Surface chemical control of mechanical energy losses in micromachined silicon structures, *J. Phys. Chem. B* **107**, 14270 (2003). [1.2.1](#), [3.3](#)
- [81] S. A. Hickman et al., Batch-fabrication of cantilevered magnets on attonewton-sensitivity mechanical oscillators for scanned-probe nanoscale magnetic resonance imaging, *ACS Nano* **4**, 7141 (2010). [1.2.1](#), [1.2.1](#), [1.3](#), [2.1](#), [2.2](#), [2.3](#), [2.1](#), [2.4](#), [2.4](#), [2.5](#), [2.6](#), [2.6](#), [3.1](#), [3.2](#), [3.3](#), [3.5](#), [3.6](#), [3.6](#), [3.8](#), [3.9](#), [4.1](#), [4.3.2](#), [5.1](#), [5.2.2](#), [5.6](#), [6.1](#)
- [82] J. G. Longenecker, E. W. Moore, and J. A. Marohn, Rapid serial prototyping of magnet-tipped attonewton-sensitivity cantilevers by focused ion beam manipulation, *J. Vac. Sci. Technol. B* **29**, 032001 (2011). [1.2.1](#), [1.3](#), [3.6](#), [5.2.2](#), [6.1](#), [6.4.3](#)
- [83] B. C. Stipe, H. J. Mamin, T. D. Stowe, T. W. Kenny, and D. Rugar, Noncontact friction and force fluctuations between closely spaced bodies, *Phys. Rev. Lett.* **87**, 096801 (2001). [1.2.1](#), [4.3](#), [5.6](#)

- [84] S. Kuehn, R. F. Loring, and J. A. Marohn, Dielectric fluctuations and the origins of noncontact friction, *Phys. Rev. Lett.* **96**, 156103 (2006). [1.2.1](#), [2.1](#), [4.3](#), [5.6](#)
- [85] S. M. Yazdanian, J. A. Marohn, and R. F. Loring, Dielectric fluctuations in force microscopy: Noncontact friction and frequency jitter, *J. Chem. Phys.* **128**, 224706 (2008). [1.2.1](#), [4.1](#), [5.5](#)
- [86] S. M. Yazdanian, N. Hoepker, S. Kuehn, R. F. Loring, and J. A. Marohn, Quantifying electric field gradient fluctuations over polymers using ultrasensitive cantilevers, *Nano Lett.* **9**, 2273 (2009). [1.2.1](#), [2.1](#), [5.5](#)
- [87] N. Hoepker, S. Lekkala, R. F. Loring, and J. A. Marohn, Quantifying dielectric fluctuations over polymer films using an atomic force microscope, *J. Phys. Chem. B* **115**, 14493 (2011). [1.2.1](#), [5.5](#)
- [88] E. W. Moore, S.-G. Lee, S. A. Hickman, L. E. Harrell, and J. A. Marohn, Evading surface and detector frequency noise in harmonic oscillator measurements of force gradients, *Appl. Phys. Lett.* **97**, 044105 (2010). [1.2.1](#), [6.1](#)
- [89] T. N. Ng, N. E. Jenkins, and J. A. Marohn, Thermomagnetic fluctuations and hysteresis loops of magnetic cantilevers for magnetic resonance force microscopy, *IEEE Trans. Mag.* **42**, 378 (2006). [1.2.2](#), [2.1](#), [2.4](#), [4.1](#), [4.3.2](#), [4.4](#), [5.2.2](#)
- [90] S.-G. Lee, E. W. Moore, and J. A. Marohn, A unified picture of cantilever frequency-shift measurements of magnetic resonance, *Phys. Rev. B* **85**, 165447 (2012). [1.2.2](#)
- [91] S. A. Hickman, *Batch Fabrication of Cantilevered Magnetic Nanorods on Attonewton-Sensitivity Silicon Oscillators for Magnetic Resonance Force Microscopy*, PhD thesis, Cornell University, 2010. [1.3](#), [2.3](#), [2.3](#), [2.4](#), [2.5](#), [3.1](#), [3.3](#), [4.1](#), [4.3.2](#), [7](#), [B](#)
- [92] T. D. Stowe, T. W. Kenny, D. J. Thomson, and D. Rugar, Silicon dopant imaging by dissipation force microscopy, *Appl. Phys. Lett.* **75**, 2785 (1999). [2.1](#)

- [93] B. C. Stipe, H. J. Mamin, T. D. Stowe, T. W. Kenny, and D. Rugar, Magnetic dissipation and fluctuations in individual nanomagnets measured by ultrasensitive cantilever magnetometry, *Phys. Rev. Lett.* **86**, 2874 (2001). [2.1](#), [2.4](#), [4.1](#), [4.4](#), [4.4](#), [5.2.2](#), [6.4.3](#)
- [94] J. Jang et al., Observation of half-height magnetization steps in Sr_2RuO_4 , *Science* **331**, 186 (2011). [2.1](#), [3.9](#)
- [95] A. C. Bleszynski-Jayich, W. E. Shanks, B. R. Ilic, and J. G. E. Harris, High sensitivity cantilevers for measuring persistent currents in normal metal rings, *J. Vac. Sci. Technol. B* **26**, 1412 (2008). [2.1](#)
- [96] A. C. Bleszynski-Jayich et al., Persistent currents in normal metal rings, *Science* **326**, 272 (2009). [2.1](#)
- [97] S. R. Garner, *Force-Gradient Detection of Nuclear Magnetic Resonance*, PhD thesis, Cornell University, 2005. [2.2](#), [6.4.1](#)
- [98] B. W. Chui et al., Mass-loaded cantilevers with suppressed higher-order modes for magnetic resonance force microscopy, 12th International Conference on Solid-State Sensors and Actuators (Transducers 2003) **2**, 1120 (2003). [2.2](#)
- [99] D. Mozyrsky, I. Martin, D. Pelekhov, and P. C. Hammel, Theory of spin relaxation in magnetic resonance force microscopy, *Appl. Phys. Lett.* **82**, 1278 (2003). [2.2](#)
- [100] G. P. Berman, V. N. Gorshkov, D. Rugar, and V. I. Tsifrinovich, Spin relaxation caused by thermal excitations of high-frequency modes of cantilever vibrations, *Phys. Rev. B* **68**, 094402 (2003). [2.2](#)
- [101] M. J. Rooks, S. Wind, P. McEuen, and D. E. Prober, Fabrication of 30-nm-scale structures for electron transport studies using a polymethylmethacrylate bilayer resist, *J. Vac. Sci. Technol. B* **5**, 318 (1987). [2.3](#)

- [102] F. Laermer and A. Schilp, Method of anisotropic etching of silicon, 2003. [2.3](#), [3.3](#)
- [103] P. Lee et al., On the Ni-Si phase transformation with/without native oxide, *Microelectron. Eng.* **51–52**, 583 (2000). [2.3](#), [4.2](#)
- [104] M. Tinani et al., In situ real-time studies of nickel silicide phase formation, *J. Vac. Sci. Technol. B* **19**, 376 (2001). [2.3](#), [2.4](#)
- [105] X. Guo et al., Study of nickel silicide formation on Si(110) substrate, *Appl. Surf. Sci.* **257**, 10571 (2011). [2.3](#), [2.4](#)
- [106] D. Lishan, Personal communication, 2012. [2.3](#)
- [107] M. Qin, M. Poon, and C. Yuen, A study of nickel silicide film as a mechanical material, *Sens. Actuators, A* **87**, 90 (2000). [2.3](#)
- [108] L. Dubois and B. Zegarski, The activated adsorption of silane on nickel, *Surf. Sci.* **204**, 113 (1988). [2.3](#)
- [109] T. Gnanavel et al., Ni and W nanotips: Fabrication and characterisation, *J. Phys.: Conf. Ser.* **126**, 012071 (2007). [2.3](#)
- [110] M. J. Graham and M. Cohen, On the mechanism of low-temperature oxidation (23–450°C) of polycrystalline nickel, *J. Electrochem. Soc.* **7**, 879 (1972). [4.2](#)
- [111] S. H. Kulpa and R. P. Frankenthal, Tarnishing of nickel in air at temperatures from 23° to 200°C and relative humidities from ambient to 95%, *J. Electrochem. Soc.* **124**, 1588 (1977).
- [112] M. R. Pinnel, H. G. Tompkins, and D. E. Heath, Oxidation of nickel and nickel-gold alloys in air at 50°–150°C, *J. Electrochem. Soc.* **126**, 1274 (1979). [2.3](#), [4.2](#)
- [113] E. J. McGuire, Photo-ionization cross sections of the elements helium to xenon, *Phys. Rev.* **175**, 20 (1968). [2.3](#)

- [114] M. Baldé, *Silicide Formation through Diffusion Barriers*, PhD thesis, University of Stellenbosch, 2005. [2.4](#)
- [115] O. Ozatay et al., Sidewall oxide effects on spin-torque- and magnetic-field-induced reversal characteristics of thin-film nanomagnets, *Nat. Mater.* **7**, 567 (2008). [2.4](#), [3.2](#)
- [116] X. Zhang, J. Zhao, A. V. Whitney, J. W. Elam, and R. P. Van Duyne, Ultrastable substrates for surface-enhanced raman spectroscopy: Al₂O₃ overlayers fabricated by atomic layer deposition yield improved anthrax biomarker detection, *J. Am. Chem. Soc.* **128**, 10304 (2006). [2.4](#), [3.2](#)
- [117] T. N. Ng, *Developments in Force Detection: Integrated Cantilever Magnetometry and Electric Force Microscopy of Organic Semiconductors*, PhD thesis, Cornell University, 2006. [2.4](#), [4.1](#)
- [118] J. Mayer, L. A. Giannuzzi, T. Kamino, and J. Michael, TEM sample preparation and FIB-induced damage, *MRS Bull.* **32**, 400 (2007). [2.6](#), [7](#)
- [119] U. Hartmann, Magnetic force microscopy, *Annu. Rev. Mater. Sci.* **29**, 5387 (1999). [2.6](#)
- [120] Z. Deng et al., Metal-coated carbon nanotube tips for magnetic force microscopy, *Appl. Phys. Lett.* **85**, 6263 (2004). [2.6](#)
- [121] M. Koblishka, U. Hartmann, and T. Sulzbach, Resolving magnetic nanostructures in the 10-nm range using MFM at ambient conditions, *Mater. Sci. Eng. C* **23**, 747 (2003). [2.6](#)
- [122] M. R. Koblishka, J. D. Wei, C. Richter, T. H. Sulzbach, and U. Hartmann, Advanced cantilevers for magnetic force microscopy and high frequency magnetic force microscopy, *Scanning* **30**, 27 (2008). [2.6](#)

- [123] S. Ingole et al., Assembly and magnetic properties of nickel nanoparticles on silicon nanowires, *Appl. Phys. Lett.* **94**, 223118 (2009). [2.6](#)
- [124] A. Winkler et al., Magnetic force microscopy sensors using iron-filled carbon nanotubes, *J. Appl. Phys.* **99**, 104905 (2006). [2.6](#)
- [125] M. Li et al., Bottom-up assembly of large-area nanowire resonator arrays, *Nat. Nanotechnol.* **3**, 88 (2008). [2.6](#)
- [126] J. Yang, T. Ono, and M. Esashi, Mechanical behavior of ultrathin microcantilever, *Sens. Actuators, A* **82**, 102 (2000). [2.6](#)
- [127] P. Panjan, D. K. Merl, F. Zupanič, M. Čekada, and M. Panjan, SEM study of defects in PVD hard coatings using focused ion beam milling, *Surf. Coat. Technol.* **202**, 2302 (2008). [3.1](#)
- [128] E. Beach, M. Keefe, W. Heeschen, and D. Rothe, Cross-sectional analysis of hollow latex particles by focused ion beam-scanning electron microscopy, *Polymer* **46**, 11195 (2005). [3.1](#)
- [129] A. Grabulov, U. Ziese, and H. Zandbergen, TEM/SEM investigation of microstructural changes within the white etching area under rolling contact fatigue and 3-D crack reconstruction by focused ion beam, *Scripta Mater.* **57**, 635 (2007). [3.1](#)
- [130] S. Abolhassani and P. Gasser, Preparation of TEM samples of metal-oxide interface by the focused ion beam technique, *J. Microsc.* **223**, 73 (2006).
- [131] F. A. Stevie et al., Application of focused ion beam lift-out specimen preparation to TEM, SEM, STEM, AES and SIMS analysis, *Surf. Interface Anal.* **31**, 345 (2001).
- [132] R. M. Langford and A. K. Petford-Long, Preparation of transmission electron mi-

- crosscopy cross-section specimens using focused ion beam milling, *J. Vac. Sci. Technol. A* **19**, 2186 (2001). [3.1](#)
- [133] E. Fawcett, Spin-density-wave antiferromagnetism in chromium, *Rev. Mod. Phys.* **60**, 209 (1988). [2](#), [4.3.2](#)
- [134] R. Hanestad, J. W. Butterbaugh, A. ben-Hamida, and I. Gelmi, Stiction-free release etch with anhydrous HF/water vapor processes, *Proc. SPIE* **4557**, 58 (2001). [3.8](#)
- [135] D. Vestyck, Personal communication, 2010. [3.8](#)
- [136] G. D. Fuchs et al., Spin-torque ferromagnetic resonance measurements of damping in nanomagnets, *Appl. Phys. Lett.* **91**, 062507 (2007). [3.9](#)
- [137] I.-C. Chen, L.-H. Chen, C. A. Orme, and S. Jin, Control of curvature in highly compliant probe cantilevers during carbon nanotube growth, *Nano Lett.* **7**, 3035 (2007). [3.9](#)
- [138] J. L. Hutter and J. Bechhoefer, Calibration of atomic-force microscope tips, *Rev. Sci. Instrum.* **64**, 1868 (1993). [4.1](#), [5.2.1](#)
- [139] J. A. Marohn, R. Fainchtein, and D. D. Smith, An optimal magnetic tip configuration for magnetic-resonance force microscopy of microscale buried features, *Appl. Phys. Lett.* **73**, 3778 (1998). [4.1](#), [4.4](#), [5.2.2](#), [6.4.3](#)
- [140] A. Aharoni, Demagnetizing factors for rectangular ferromagnetic prisms, *J. Appl. Phys.* **83**, 3432 (1998). [4.1](#)
- [141] E. S. Lambers, C. N. Dykstal, J. M. Seo, J. E. Rowe, and P. H. Holloway, Room-temperature oxidation of Ni(110) at low and atmospheric oxygen pressures, *Oxid. Met.* **45**, 301 (1996). [4.2](#)

- [142] W. H. Meiklejohn and C. P. Bean, New magnetic anisotropy, *Phys. Rev.* **102**, 1413 (1956). [4.3.2](#)
- [143] L. Smardz, U. Köbler, and W. Zinn, Oxidation kinetics of thin and ultrathin cobalt films, *J. Appl. Phys.* **71**, 5199 (1992). [4.3.2](#)
- [144] D. A. Shirley, High-resolution X-ray photoemission spectrum of the valence bands of gold, *Phys. Rev. B* **5**, 4709 (1972). [4.3.4](#)
- [145] K. J. Bruland et al., Thermal tuning of a fiber-optic interferometer for maximum sensitivity, *Rev. Sci. Instrum.* **70**, 3542 (1999). [5.2.1](#)
- [146] J. P. Jacky, J. L. Garbini, M. Ettus, and J. A. Sidles, Digital control of force microscope cantilevers using a field programmable gate array, *Rev. Sci. Instrum.* **79**, 123705 (2008). [5.2.1](#)
- [147] T. R. Albrecht, P. Grütter, D. Horne, and D. Rugar, Frequency modulation detection using high-Q cantilevers for enhanced force microscope sensitivity, *J. Appl. Phys.* **69**, 668 (1991). [5.2.1](#), [5.5](#)
- [148] J. A. Sidles, J. L. Garbini, W. M. Dougherty, and S.-H. Chao, The classical and quantum theory of thermal magnetic noise, with applications in spintronics and quantum microscopy, *Proc. IEEE* **91**, 799 (2003). [5.6](#)
- [149] M. Giorgio, B. Meier, R. Magin, and E. Meyer, Magnetic damping losses of tipped cantilevers, *Nanotechnology* **17**, 871 (2006). [5.6](#)
- [150] S. Kuehn, J. A. Marohn, and R. F. Loring, Noncontact dielectric friction, *J. Phys. Chem. B* **110**, 14525 (2006). [5.6](#)
- [151] J. Labaziewicz et al., Temperature dependence of electric field noise above gold surfaces, *Phys. Rev. Lett.* **101**, 180602 (2008). [5.6](#)

- [152] R. G. Griffin and T. F. Prisner, High field dynamic nuclear polarization — the renaissance, *Phys. Chem. Chem. Phys.* **12**, 5737 (2010). [6.1](#)
- [153] T.-M. Chuang et al., Nematic electronic structure in the parent state of the iron-based superconductor $\text{Ca}(\text{Fe}_{1-x}\text{Co}_x)_2\text{As}_2$, *Science* **336**, 181 (2010). [6.2](#)
- [154] M. P. Allan et al., Anisotropic energy gaps of iron-based superconductivity from intraband quasiparticle interference in LiFeAs , *Science* **336**, 563 (2012). [6.2](#)
- [155] J. E. Hoffman, *A Search for Alternative Electronic Order in the High Temperature Superconductor $\text{Bi}_2\text{Sr}_2\text{CaCu}_2\text{O}_{8+\delta}$ by Scanning Tunneling Microscopy*, PhD thesis, University of California, Berkeley, 2003. [6.2.1](#)
- [156] M. Poggio, Personal communication, 2012. [6.2.2](#)
- [157] R. C. Richardson and E. N. Smith, editors, *Experimental Techniques in Condensed Matter Physics at Low Temperatures*, Addison-Wesley, 1998. [6.3.1](#), [6.3.3](#)
- [158] E. W. Moore, *1. Mechanical Detection of Electron Spin Resonance from Nitroxide Spin Probes, 2. Ultrasensitive Cantilever Torque Magnetometry of Magnetization Switching in Individual Nickel Nanorods*, PhD thesis, Cornell University, 2011. [6.3.2](#), [6.4.5](#)
- [159] D. Rugar, H. Mamin, and P. Guethner, Improved fiber-optic interferometer for atomic force microscopy, *Appl. Phys. Lett.* **55**, 2588 (1989). [6.4.1](#)
- [160] A. L. Woodcraft, Recommended values for the thermal conductivity of aluminium of different purities in the cryogenic to room temperature range, and a comparison with copper, *Cryogenics* **45**, 626 (2005). [6.4.2](#)
- [161] E. Gmelin, M. Asen-Palmer, M. Reuther, and R. Villar, Thermal boundary resistance of mechanical contacts between solids at sub-ambient temperatures, *J. Phys. D: Appl. Phys.* **32**, R19R43 (1999). [6.4.2](#)

- [162] F. Xue, P. Peddibhotla, M. Montinaro, D. P. Weber, and M. Poggio, A geometry for optimizing nanoscale magnetic resonance force microscopy, *Appl. Phys. Lett.* **98**, 163103 (2011). [6.4.3](#)
- [163] J. A. Marohn, Magnetic resonance force microscopy tutorial, 3rd International Conference on Nano Magnetic Resonance Imaging; Le Tremblay-sur-Mauldre, France; July 12 – 16, 2010. [6.4.3](#)
- [164] S. H. Pan, International patent publication no. wo 93/19494, Technical report, 1993. [6.4.4](#)
- [165] C. Wittneven, R. Dombrowski, S. H. Pan, and R. Wiesendanger, A low-temperature ultrahigh-vacuum scanning tunneling microscope with rotatable magnetic field, *Rev. Sci. Instrum.* **68**, 3806 (1997).
- [166] A. Gupta and K. Ng, Compact coarse approach mechanism for scanning tunneling microscope, *Rev. Sci. Instrum.* **72**, 3552 (2001). [6.4.4](#)
- [167] J. A. Sidles, R. Picone, J. Garbini, and J. Jacky, Transport mechanisms for inducting dynamic nuclear hyperpolarization in magnetic resonance microsystems: Dynamical theory, design rules, and experimental protocols, Technical report, UW Quantum Systems Engineering (QSE) Group, University of Washington, Seattle, WA, 2011. [6.5](#)
- [168] D. Gill and N. Bloembergen, Linear Stark splitting of nuclear spin levels in GaAs, *Phys. Rev.* **129**, 2398 (1963). [7](#)
- [169] R. W. Dixon and N. Bloembergen, Electrically induced perturbations of halogen nuclear quadrupole interactions in polycrystalline compounds. II. Microscopic theory, *J. Chem. Phys.* **41**, 1739 (1964). [7](#)
- [170] J. A. Marohn et al., Optical Larmor beat detection of high-resolution nuclear magnetic resonance in a semiconductor heterostructure, *Phys. Rev. Lett.* **75**, 1364 (1995). [7](#)

- [171] J. G. Kempf, M. A. Miller, and D. P. Weitekamp, Imaging quantum confinement with optical and POWER (perturbations observed with enhanced resolution) NMR, Proc. Natl. Acad. Sci. U.S.A. **105**, 20124 (2008). [7](#)
- [172] T. G. Frey, G. A. Perkins, and M. H. Ellisman, Electron tomography of membrane-bound cellular organelles, Annu. Rev. Biophys. Biomol. Struct. **35**, 199 (2006). [7](#)
- [173] N. Urushihara et al., Three dimensional image construction and spectrum extraction from two dimensional elemental mapping in Auger electron spectroscopy, J. Vac. Sci. Technol. A **26**, 668 (2008). [7](#)
- [174] M. Hemmous, A. Layadi, A. Guittoumb, A. Bourzami, and A. Benabbas, Effect of deposition rate and thickness on the structural and electrical properties of evaporated Ni/glass and Ni/Si(100) thin films, Microelectron. J. **39**, 1545 (2008). [7](#)
- [175] Y. Wang, S. A. Boden, D. M. Bagnall, H. N. Rutt, and C. H. de Groot, Helium ion beam milling to create a nano-structured domain wall magnetoresistance spin valve, Nanotechnology **23**, 395302 (2012). [7](#)